PLOS Computational Biology

RESEARCH ARTICLE

Simultaneously determining regional heterogeneity and connection directionality from neural activity and symmetric connection

Jiawen Chang[1,2], **Zhuda Yang**[1,2], **Changsong Zhou**[1,2,3]*

1 Department of Physics, Hong Kong Baptist University, Kowloon Tong, Hong Kong, **2** Centre for Nonlinear Studies, Hong Kong Baptist University, Kowloon Tong, Hong Kong, **3** Life Science Imaging Centre, Hong Kong Baptist University, Kowloon Tong, Hong Kong

* cszhou@hkbu.edu.hk

Abstract

The spatiotemporal patterns of neural dynamics are jointly shaped by directed structural interactions and heterogeneous intrinsic features of the neural components. Despite well-developed methods for estimating directionality in network connections from network of homogeneous nodes, how local heterogeneity impacts on directionality estimation remains poorly understood. In particular, the role of excitatory-inhibitory interactions in shaping network directionality and how these interactions should be incorporated into reconstruction frameworks remain largely unexplored. Here, we present a novel reconstruction framework that simultaneously estimates effective heterogeneity across network nodes and asymmetric network connections from neural activity and symmetric connection, both are assessible in experimental data, validated using macaque cortical connectivity data and several circuit models. We found that the estimated local heterogeneity remains consistent across various forms of parameterized local circuit heterogeneity. Furthermore, we demonstrated and quantified how hidden local inhibitory populations only modify within-region connection strengths, elucidating the functional equivalence between dynamics of excitatory-inhibitory networks and purely observing excitatory networks when estimating effective heterogeneity and asymmetry. Finally, we demonstrated the sampling interval effect in estimating network interactions with respect to the sampling resolution. Together, our results not only provide a unified framework for evaluating relative functional contributions of local heterogeneity and asymmetry to overall system dynamics but also reveal the fundamental limitations and scaling principles in reconstructing neural circuit connectivity from experimental observations.

OPEN ACCESS

Citation: Chang J, Yang Z, Zhou C (2025) Simultaneously determining regional heterogeneity and connection directionality from neural activity and symmetric connection. PLoS Comput Biol 21(10): e1013612. https://doi.org/10.1371/journal.pcbi.1013612

Editor: Mikail Rubinov, Vanderbilt University, UNITED STATES OF AMERICA

Received: May 5, 2025

Accepted: October 12, 2025

Published: October 23, 2025

Peer Review History: PLOS recognizes the benefits of transparency in the peer review process; therefore, we enable the publication of all of the content of peer review and author responses alongside final, published articles. The editorial history of this article is available here: https://doi.org/10.1371/journal.pcbi.1013612

Data availability statement: The Macaque Cortex dataset is publicly available at https://doi.org/10.1016/j.neuron.2015.09.008 Raw datasets can be accessed at http://core-nets.org/ (free registration required). Upon logging in, users can directly access and download the following datasets from the main page: 1. Empirical structural connectivity: "A weighted and directed interareal connectivity matrix for macaque cerebral cortex" (Markov NT, et al., Cereb Cortex. 2014 Jan;24(1):17-36). 2. Anatomical hierarchy: "The Anatomy of Hierarchy: Feedforward and feedback pathways in macaque visual cortex" (Markov NT, et al., J Comp Neurol. 2014 Feb;522(1):225-59. doi: 10.1002/cne.23458). All code and datasets used in this study are available at: https://github.com/JiawenChang118/BrainModelling.

Funding: This work was partially supported by Science and Technology Innovation 2030-Major Projects (No. 2022ZD0208500 to C.Z.), the Hong Kong Research Grant Council (RGC) Senior Research Fellow Scheme (SRFS2324-2S05 to C.Z.), General Competitive Fund (GRF12202124 to C.Z.), and Hong Kong Baptist University (HKBU) Seed Funding for Collaborative Research Grants (RC-SFCRG/23-24/SCI/06 to Changsong Zhou). The funders had no role in study design, data collection and analysis, decision to publish, or preparation of the manuscript.

Competing interests: The authors have declared that no competing interests exist.

Author summary

How heterogeneous brain regions communicate via directed connectivity to shape the neural dynamics patterns is a fundamental question in neuroscience. Traditional methods for estimating connectivity patterns from neural activity often assume all brain regions are homogeneous. However, how this regional heterogeneity due to anatomical difference impacts on directed connectivity estimation remains an open question. Here, we developed an approach that can simultaneously identify the direction of connectivity between regions and regional properties from existing brain activity data, which we validated using macaque brain connectivity data and different biological neurodynamic models. We found that our estimates of regional heterogeneity remain consistent across various types of circuit complexity. We further demonstrated robustness of this method when facing two key limitations: the inability to directly measure inhibitory neurons, revealing the functional equivalence between networks with and without inhibitory components and the effect of sampling resolution on network estimation.

Introduction

The biophysical large-scale dynamics of the whole brain cortex are shaped by inter-areal connections and the intrinsic local circuit properties of each brain region. At the microscale, neurons within neural circuits interact and entangle, forming neuronal populations with spatially distributed anatomical features, such as neurotransmitter receptor profiles [1–4], neuron density [5,6] and myelin content [7–9]. These features collectively contribute to the heterogeneity of brain regions at the macroscale [10,11]. Meanwhile, information transmission follows the fundamental rule that signals propagate via synapses from presynaptic to postsynaptic neurons, primarily through axons and dendrites [12,13]. Consequently, long-range white matter connections inherently reflect the directionality of true asymmetric structural connectivity (SC), which describes the neural interactions between cortical areas [14,15]. The intricate interplay between directional structural connectivity and local heterogeneity shapes the complex large-scale dynamics of the brain, emphasizing the importance of considering both factors to more comprehensively understand neural information flow and processing [16–19].

Developments in magnetic resonance imaging (MRI) have provided a noninvasive method to measure human brain heterogeneity and connectivity, both structural and functional, at the whole brain level. *In vivo* studies have found and revealed abundant anatomical heterogeneity content, e.g., contrast ratio of T1- to T2-weighted maps can reflect the intracortical myelination [7–9,20]. Information of SC is obtained through diffusion MRI (dMRI) and tractography methods, which estimate the density of white matter fibers connecting different brain regions [21–23]. However, SC obtained from dMRI does not contain directionality of the connection, which strongly limit our understanding of information processing in the brain network. Functional connectivity (FC) measures the temporal correlations between neural activity in these regions, typically calculated using resting-state functional magnetic resonance imaging (fMRI) data which captures blood oxygen level-dependent (BOLD) signals to represent neural synchronization dependence, again without the directionality of interaction [24]. Furthermore, these methods are not well-suited in quantifying the precise contribution of anatomical heterogeneity to brain dynamics and function, especially its interplay with the directionality of structural connectivity underlying information transmission [25].

Inferred from observed neural activity under assumed generative models, causal influences between cortical areas provide valuable insights into network interactions [26]. Various methods have been developed to estimate these influences, often referred to as effective connectivity (EC): Dynamic Causal Modeling, based on a Bayesian framework, primarily estimates latent neural quantities from measured brain activity [27–30]; perturbation studies systematically alter neural activity in specific nodes to map causal influences and information flow [31–33]; and noise-correlation analysis approaches establish relationships between SC and statistical quantities of neural activity (e.g., FC, covariance, and differential covariance) [34,35]. These methods collectively aim to capture the directional nature of information flow in brain networks, revealing causal relationships between regions of interest (ROIs) that go beyond simple activity correlations. However, these approaches often do not adequately account for local heterogeneity, which is also a key aspect contributing to dynamics and information processing [36–39], potentially resulting in estimated directional EC that may confound local heterogeneity with true directional connectivity. It is thus important to develop methods that can simultaneously estimate both local heterogeneity and connection asymmetry to more accurately characterize the directionality of connections in neural networks.

In this study, we propose a framework to simultaneously reconstruct node heterogeneity and asymmetry connections of brain networks, by extending the existing Dynamical Differential Covariance (DDC) method [35] initially developed for homogeneous nodes. We evaluated the reconstruction performance across a wide range of parameters on well-developed large-scale circuit models constrained by ground truth asymmetric macaque cortical connectivity and regional heterogeneity [36,37,40,41]. Firstly, this method systematically identifies effective local heterogeneity and asymmetric SC based on neural dynamics and symmetric SC, which are both accessible in empirical data, without requiring prior knowledge of SC directionality. We found that the effective heterogeneity identified by this method can further reconstruct various types of parameterized local heterogeneity across different models, such as self-recurrent strength, external input current, time constant, and firing threshold, enabling comparisons of the dynamical properties associated with different forms of local heterogeneity. We then demonstrated that this reconstruction method can effectively estimate the mixed effects involving hidden local inhibitory populations within a detailed excitatory-inhibitory network activity into effective excitatory-excitatory interactions in the regime below bifurcation to oscillatory states. Furthermore, we demonstrated a sampling interval effect on the reconstruction and separation of heterogeneity and asymmetry, considering the mismatch between observed data sampling rates and underlying neural dynamics temporal resolution. Together, our results provide a theoretical framework for reconstructing brain heterogeneity and connection asymmetry, and suggest a unified expression for further analysis of the relative contributions of local heterogeneity and asymmetric connections to neural network dynamics. The framework is extendable to other dynamical networks beyond neural systems.

Results

I. A unified framework of regional heterogeneity and asymmetric structural connections

The EC of the nervous system, inferred from neural activity, not only describes the strength of interactions between areas or neurons but also reveals the direction of information flow from one to another [28–34]. This directionality emerges from two key factors: the anatomical asymmetry structure of connections and the intrinsic properties of brain regions. Regional heterogeneity quantifies spatial variation across areas, establishing each region's hierarchical position and processing specialization, while asymmetry measures directional imbalances between feedforward and feedback pathways, revealing connection strength patterns and network topology [10,15]. However, little is discussed regarding how these two factors

-- anatomical direction of inter-areal interactions and the heterogeneous features within areal properties – jointly influence the directionality of EC.

In this section, we describe a unified framework for representing regional heterogeneity and asymmetric connections. As the choice of regional heterogeneity relies on the model, without loss of generality, we started by following existing studies on heterogeneous large-scale brain network model [35,40]. For each ROI in total of *N* regions, the large-scale circuit model describes the neural activity in the following dynamics:

$$\frac{dS_i}{dt} = -\frac{S_i}{\tau_s} + \gamma\left(1 - S_i\right) H\left(x_i\right) + \sigma\nu_i(t), \tag{1}$$

$$H\left(x_i\right) = \frac{ax_i - b}{1 - \exp\left(-d\left(ax_i - b\right)\right)}, \tag{2}$$

$$x_i = w_i S_i + G\Sigma_j C_{ij} S_j + I_i, \tag{3}$$

where $S_i(t)$ is the synaptic gating variable of region *i*. τ_s are the kinetic parameters controlling the decay time and γ is scaling factor. $v_i(t)$ is independent standard Gaussian noise term with amplitude σ at each ROI. The population firing rate (or activation function) $H(x_i)$ of region *i* is defined as a function of total input current x_i, with gain factor *a*, threshold *b* and parameter *d* controlling the nonlinearity [42].

We utilized an open dataset containing directed SC and anatomical heterogeneity across macaque cortical areas to establish ground truth asymmetric SC and parameter heterogeneity [10,15,43]. C_{ij} is asymmetric SC matrix describing anatomical connection from region *j* to *i* in total *N* regions, ranging from primary sensory cortex to higher order cortex [10,15] [Materials and Method]. Following previous studies [36,41], local recurrent strength w_i, and external input I_i were assumed to be heterogeneous across different regions (Fig 3A). Local recurrent strength w_i is rescaled from empirical anatomical heterogeneity [Materials and Method]. The values of parameters in Eqs 1–3 are provided in Table 1 following previous studies [36,40–43].

To directly link how regional heterogeneity and asymmetry contribute to the whole network dynamics, we linearized the model of Eqs 1–3 by performing the first-order Taylor expansion around its stable states [40,44]. This results in the Jacobian matrix governing the linear neural dynamic [Materials and Method]:

$$\frac{dS}{dt} = J\left(S^*\right)\left(S - S^*\right) + \sigma\nu(t), \tag{4}$$

Table 1. Fixed parameters for large-scale circuit model.

Parameter	Value	Reference
τ_s	0.1 *s*	[40]
γ	0.641	[40]
σ	0.01	[40]
a	270 nC^{-1}	[40]
b	108 Hz	[40]
d	0.154 *s*	[40]
w_i	0.0652-0.1581 *nA*	[36,43]
I_i	0.30-0.35 *nA*	[36]

https://doi.org/10.1371/journal.pcbi.1013612.t001

where $J(S^*)$ is the Jacobian matrix around the fixed point S^*. In the linear case, this Jacobian matrix represents EC. The elements in the Jacobian matrix quantify how local neural activity dynamics emerge from the interplay between asymmetric SC and regional heterogeneity (defined in Eq. 19).

By evaluating this Jacobian around fixed points (Eq. 4), we explicitly relate anatomical connection strengths (SC weights) and node-specific properties (state-dependent effective heterogeneity) to functional interactions governing activity patterns. Here, we propose that the directionality of the Jacobian J (i.e., $J(S^*)$) can be expressed in the generic form of Eq. 5 below, with contribution from regional effective heterogeneity h_i and asymmetric SC C_{ij} between two regions:

$$J_{ij} = h_i C_{ij}, \;\; i \neq j, \tag{5}$$

and in the case of the model in Eqs 1–3,

$$h_i = \gamma G \left(1 - S_i^*\right) \frac{\partial H}{\partial x_i} \;\; |_{x_i = x_i^*} \;, \tag{6}$$

and the diagonal elements of the Jacobian $J_{ii} = -\frac{1}{\tau_S\left(1 - S_i^*\right)} + \frac{w_i h_i}{G}$ [Materials and Method]. $x_i^* = w_i S_i^* + G \Sigma_j C_{ij} S_j^* + I_i$ is the steady total input.

This formula for both representing effective regional heterogeneity and asymmetric connections described by Eq. 5 is not restricted to a specific dynamical model but is a unified framework that can encompass a broad range of heterogeneous dynamic models [36–38,41]. Table 2 presents the expression of effective heterogeneity h_i across different models, as discussed in the subsequent reconstruction procedure.

In all models, S_i^* and x_i^*represent the steady state solution and steady overall external current of region i respectively. x_i' and $x_{i,E}^*$ have different notations because their formula are different from Model A. In Model B, the effective heterogeneity h_i is determined by both the heterogeneous activation function H_i and the overall input x_i' [Materials and Method]. Model B combines various parameterized local heterogeneities $\{\tau_i, b_i\}$ in contrast to Model A which has $\{w_i, I_i\}$ (see Section V). In Model C, the effective heterogeneity h_i is determined by both the parameterized local heterogeneities and the interactions between excitatory and inhibitory populations (see Section V).

The following sections systematically demonstrate and validate our framework. We first show how to reconstruct the effective heterogeneity h_i and asymmetric SC C_{ij} from the neural activity $S_i(t)$ and symmetric SC W_{ij} in section II, where we assume $W_{ij} = \frac{C_{ij} + C_{ji}}{2}$ and can be obtained from dMRI. We also evaluate the accuracy of our reconstruction method based on Model A (Eqs 1–3) under different parameter conditions in section III.

Our proposition above demonstrates that the reconstructed effective heterogeneity h_i is typically influenced by both the system's steady state S^*, the firing rate change (gain function level) $\frac{\partial H}{\partial x_i} \;\; |_{x_i = x_i^*}$, as well as the parameterized anatomical heterogeneity, including the local recurrent strength w_i and external input I_i. We discuss how to use the effective heterogeneity h_i to reconstruct the parameterized anatomical heterogeneity w_i and I_i in section IV. In section V, we present how our proposed effective heterogeneity can be derived from different combinations of heterogeneous parameters, representing a unified framework: when studying EC, effective heterogeneity characterizes the dynamical contributions of heterogeneity based on different empirical data sources. Finally, in section VI, we propose the sampling interval effect, systematically

Table 2. Expressions of effective heterogeneity h_i across different models.

Models	Reference	Population(s)	*hi*
A	Kong et al. (2021) [36]	*E*	$\gamma G \left(1 - S_i^*\right) \frac{\partial H}{\partial x_i} \;\; |_{x_i = x_i^*}$
B	Adapted from Deco et al. (2021) [37]	*E*	$\gamma G \left(1 - S_i^*\right) \frac{\partial H_i}{\partial x_i} \;\; |_{x_i = x_i'}$
C	Demirtas et al. (2019) [38]	*E, I*	$(E):\; \gamma G \left(1 - S_{i,E}^*\right) \frac{\partial H_E}{\partial x_i} \;\; |_{x_{i,E} = x_{i,E}^*}$

https://doi.org/10.1371/journal.pcbi.1013612.t002

quantifying how the true structural connectivity and effective heterogeneity are affected by the sampling window during the estimation of EC under sampled neural activity.

II. Neural activity-driven reconstruction method of regional heterogeneity and asymmetric connection

We developed a data-driven method to disentangle and identify two key components: the underlying effective local heterogeneity h_i and asymmetric SC C_{ij} following the generic framework in Eqs 4 and 5. This method requires only neural activity data and symmetric SC information, both of which are commonly available from whole-brain imaging studies. Briefly, our heterogeneity and asymmetry reconstruction framework consist of two parts: temporal reconstruction and spatial reconstruction (Fig 1). For the temporal reconstruction, we estimated the Jacobian matrix J from the neural activity S, and for the spatial reconstruction, we inferred the regional heterogeneity h and asymmetric SC C based on estimated J and symmetric SC $W = \frac{C+C^T}{2}$. We assumed that W can be regarded as connectivity obtained in dMRI [21–23].

During temporal reconstruction (Fig 1A), we employed the DDC method to decode the directionality from neural activity data based on Eq. 4 and infer the underlying Jacobian J representing the spatial network structure [35]. The DDC method provides an unbiased estimation of the directionality of Jacobian matrix by assuming that the observed neural activity arises from fluctuations around the stable fixed point in a noise-driven linear dynamical system in the form of Eq. 4. This approach derives EC through least square minimization, making it both computationally efficient and robust to noise [Materials and Method]:

$$\hat{J} = < \frac{dS}{dt}, S > < S, S >^{-1}. \tag{7}$$

We then employed spatial reconstruction with an empirical symmetric SC constraint to disentangle the effective heterogeneity h_i and asymmetric SC C_{ij} from the estimated Jacobian $\hat{J}_{ij}$ (Fig 1B and 1C). This constraint aligns with the

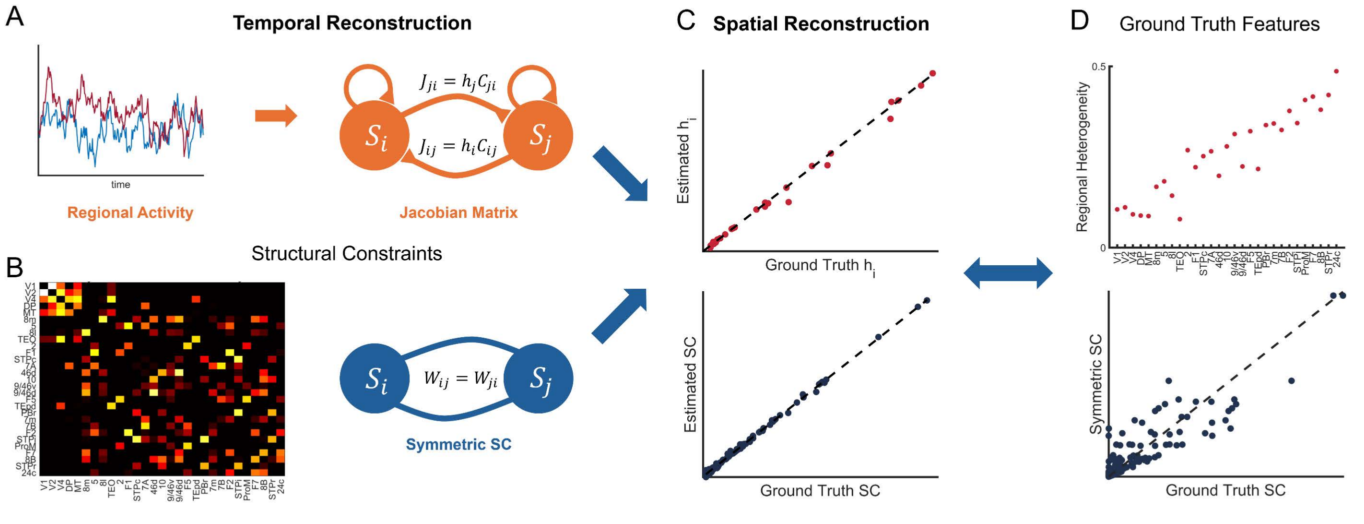

Fig 1. Schematic diagram of reconstruction. (A) Temporal Reconstruction. Neural activity $S(t)$ is transformed into a Jacobian matrix via Dynamical Differential Covariance (DDC) which provides an unbiased estimation of network coupling Jacobian J_{ij}. The Jacobian matrix (EC) here can be further divided into effective heterogeneity h_i and asymmetric SC C_{ij}. **(B)** Symmetric SC $W_{ij} = \frac{C_{ij}+C_{ji}}{2}$, is considered as structural constraints for spatial reconstruction. **(C)** Spatial reconstruction further separates effective heterogeneity h_i (top) and asymmetric SC C_{ij} (bottom) following the temporal reconstruction and structural constraints. **(D)** The effective heterogeneity h_i represents an example calculated using Eq. 6. (Bottom) The systematic difference between ground truth asymmetric SC and symmetric SC approximation, with asymmetry level $\eta(C) = 0.7$, representing that this empirical SC is symmetry-dominated but regulated by asymmetric connections. $\eta(C)$ is calculated as the element-wise correlation between the upper and lower triangular matrices.

https://doi.org/10.1371/journal.pcbi.1013612.g001

properties of the acquired data, as structural connectivity derived from dMRI is inherently symmetric [21–23]. We define symmetric SC as the symmetric counterpart of the asymmetric SC: $W=\frac{C+C^T}{2}$. This results in the following overdetermined equations (for sufficiently large N):

$$\begin{cases} h_i C_{ij} = \hat{J}_{ij} \\ \frac{C_{ij}+C_{ji}}{2} = W_{ij} \end{cases}, \ i \neq j. \tag{8}$$

Let $y_i=\frac{1}{h_i}$, we can reshape Eq. 8 into the form of a multivariate linear regression to estimate $\hat{y}_i$ [Materials and Method], then we can estimate the effective heterogeneity and asymmetric SC:

$$\begin{cases} \hat{h}_i = \frac{1}{\hat{y}_i} \\ \hat{C}_{ij} = \hat{y}_i \hat{J}_{ij} \end{cases}. \tag{9}$$

The estimation of the Jacobian $\hat{J}$ provides information about the network directionality inferred from neural activity, whereas the symmetric structural connectivity W indicates the presence and strength of connections.

In summary, temporal reconstruction (Eq. 7) decodes dynamical directionality, while spatial reconstruction (Eq. 9) further disentangles anatomical asymmetry and heterogeneity. This method combines observed neural activity with empirical symmetric connectivity to simultaneously recover both asymmetric structural connectivity and effective regional heterogeneity.

III. Robustness of reconstruction in parameter exploration

To evaluate the accuracy of our reconstruction method in distinguishing and revealing connectivity asymmetry and regional heterogeneity, we applied it to Model A (Eqs 1–3), which biophysically describes resting-state activity in cortical areas. Motivated by previous studies that employ global coupling strength G to tune the dynamical regime for optimal empirical fits [36–38,40,41] and noise strength σ to test the noise tolerance [35], we explored different values of G and σ. For each parameter condition, we simulated the neural activity and calculated the ground truth Jacobian matrix J_{ij} and effective heterogeneity h_i according to Eqs 19 and 6 [Materials and Method]. The simulated neural activity and symmetric SC were then used for the reconstruction procedure and validation as described in Fig 1A and 1C. The estimated features—Jacobian matrix $\hat{J}_{ij}$, asymmetric SC $\hat{C}_{ij}$, and effective heterogeneity $\hat{h}_i$ were then compared.

We evaluated the reconstruction performance for EC J_{ij}, asymmetric SC C_{ij} and effective heterogeneity h_i on model A by calculating the relative error (RE) between estimated and empirical features: $RE(a)=\frac{\|a_{emp}-a_{est}\|}{\|a_{emp}\|}$. We studied RE as a function of global coupling strength G, noise strength σ, and time length in neural activity (Figs 2 and S2).

The relative errors between the ground truth and the estimates of the Jacobian matrix J_{ij}, asymmetric SC C_{ij} and effective heterogeneity h_i decreased as the global coupling strength G increased (Fig 2A–2C, red lines). This behavior arises because higher G corresponds to a more globally integrated state of the system, where neural activity inherently encodes more information about the underlying asymmetric connections. This can be explained with Eqs 4 and 5 where the dynamic is controlled by the Jacobian matrix J and the white noise η: larger G can bring larger contribution to the activity fluctuation $\frac{dS}{dt}$ from the dynamics than the noise, reducing the noise effect in estimating $\hat{J}_{ij}$.

We systematically tested the consequences of ignoring key model features by comparing reconstruction performance under different assumptions. When estimating effective heterogeneity h_i while ignoring ground truth asymmetry (namely assuming connectivity is symmetrical), baseline comparison shows consistently high relative errors around 0.5 (Fig 2B, blue line), whereas our full framework typically achieves <0.2 at non-localized states ($G>0.3$). Similarly, when estimating asymmetric SC while ignoring ground truth heterogeneity (namely assuming homogeneous nodes), baseline comparison shows higher relative errors at high levels of G (Fig 2C, yellow line). We also note that this baseline relative error

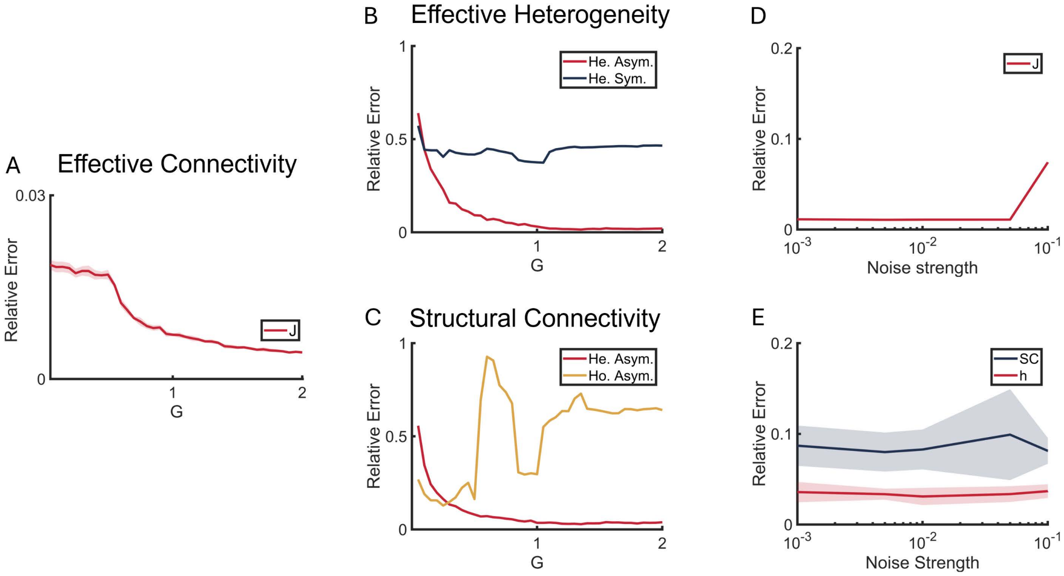

Fig 2. Robustness of reconstruction in effective heterogeneity and asymmetry. (A) The relative errors between ground truth and estimation of EC (Jacobian in Eq. 9) as functions of the global coupling strength G. **(B and C)** The relative errors of effective heterogeneity h_i (B) and asymmetric SC C_{ij} (C) revealed by the reconstruction method as functions of G. Red line represents reconstruction considering both heterogeneity and asymmetry. Blue line is baseline comparison ignoring asymmetry **(B)**. Yellow line is baseline comparison ignoring heterogeneity **(C)**. **(D)** The relative errors of Jacobian as function of noise strength σ. **(E)** The relative errors of asymmetric SC C_{ij} (blue) and regional heterogeneity h_i (red) as functions of σ. The colored lines show the mean relative errors across 10 simulations, with shaded areas indicating one standard deviation from the mean. Simulation length 50,000*s*.

https://doi.org/10.1371/journal.pcbi.1013612.g002

fluctuation is similar to the standard deviation (SD) of h_i across regions (low SD indicates that h_i values are nearly identical across regions, while high SD indicates substantial heterogeneity) (S1C Fig). This pattern suggests that systematic errors are strongly influenced by the relative heterogeneity level, while our framework demonstrates substantially better performance.

REs of EC (Jacobian), SC and effective heterogeneity as functions of noise strength σ remained consistently low across the range of σ but RE of EC slightly increased at $\sigma = 0.1$ (Fig 2C and 2D). This increase can also be explained by the fact that larger noise strength σ will enlarge the bias in the activity fluctuation $\frac{dS}{dt}$ as in Eq. 4, and therefore degrade the estimation accuracy of EC (Eq. 7). Based on this, we selected $\sigma = 0.01$ as optimal value for our simulations to ensure the system is appropriately noise-driven [36,37].

A previous study of DDC has examined how data size affects estimation accuracy [35]. To evaluate this effect on our reconstruction performance, we compared the reconstructed features across different data lengths. The relative error decreased as the data length increased from 100s to 50,000s (S1 Fig), confirming that longer recordings lead to more accurate reconstructions.

To further validate our framework's capability, we tested whether the framework can correctly identify the directionality of EC contributed by heterogeneity and/or asymmetry across various ground truth conditions, namely the ground truth models may or may not contain heterogeneity and/or asymmetry. Results demonstrated that our framework maintains comparable performance in recovering true effective heterogeneity and connectivity patterns as global coupling strength increases (S2 Fig), validating its capacity to accurately distinguish between different sources of directional connectivity.

To assess method-independence, we compared our DDC-based approach with Lyapunov optimization (LO) for EC estimation [45]. LO uses gradient descent to solve for the EC that corresponds to observed covariance, based on the Lyapunov equation constraint in linear dynamics. Results confirm that our framework's performance is robust across different

EC estimation methods, with DDC providing computational advantages particularly under high coupling conditions where the LO method faces convergence challenges (S3 Fig).

Together, these results highlight the robustness of the reconstruction method across a broad range of model architecture, parameter spaces and data constraints, underscoring its potential for reliable inference under varying experimental conditions.

IV. Detailed reconstruction of heterogeneous parameters

In this section, we investigated the mapping relationship between estimated effective heterogeneity h_i (Eq. 6) and specific parameterized local heterogeneity w_i and I_i in dynamical Model A (Fig 3A). Notably, compared to the diagonal elements of EC J_{ii}, the parameter w_i represents regional self-connections while I_i captures external inputs such as subcortical influences (Materials and Method, Eqs 28 and 30). Estimating these two heterogeneity parameters provides more biologically meaningful interpretations of neural circuit dynamics.

We first evaluated the reconstruction performance of local recurrent strength w_i and external input I_i from effective heterogeneity h_i in Model A as functions of global coupling strength G. The detailed reconstruction of local recurrent strength $\hat{w}_i$ was derived using h_i and the diagonal elements of $\hat{J}$, and the external input $\hat{I}_i$ was computed by determining the fixed total input x_i^* from firing rate change $\frac{dH}{dx_i}|_{x_i^*}$ (Materials and Method, Eqs 28–30).

At low levels of G, the relative errors of both w_i (blue) and I_i (red) decreased as G increased (Fig 3B), consistent with our findings from the spatial reconstruction of h_i and C_{ij} (Fig 2B). However, at higher values of G, the relative error of I_i began to increase (Fig 3B, red).

It was reported that the best fit between model FC and empirical FC lies around the bifurcation point in the same model A [40]. To better understand how our reconstruction framework performs near this bifurcation, which represents a highly nonlinear regime, and to explain the poor reconstruction performance at both low and high levels of G, we examined three representative conditions: localized dynamics (where the dynamics only slightly departure from the quiescent fixed point at low global coupling strength $G = 0.1$, Fig 3B, red square); the first bifurcation (where the dynamics start to exhibit bistability at $G = 0.8$, blue circle); and the second bifurcation (where the dynamics bistability is about to vanish at global scale at $G = 1.3$, yellow triangle). Bistability was detected by simulating Model A at both low and high initial states to see whether each region would converge to distinct stable states across G (S4A Fig).

Near the first bifurcation dynamics states, the firing rate change (gain function level) $\frac{dH}{dx_i}|_{x_i^*}$ were widely distributed within the linear range with some regions exhibited in the nonlinear regime (Fig 3C, blue circle).

However, in both extreme states at low and high levels of G, the firing rates are biased towards nonlinear regimes: near the second bifurcation, most ROIs operate in the upper saturation region (Fig 3D, yellow triangle), while in localized dynamics (red square), firing rates cluster near the lower threshold region. When operating in these nonlinear regions, small perturbations —such as noise in estimating the EC—may bias the estimation of $\hat{y}_i$ and $\frac{\partial H}{\partial x_i}|_{x_i^*}$. This can lead to large errors in reconstructing x_i^*, therefore introducing bias in the estimation of $\hat{I}_i$ due to the high sensitivity to noise in these regimes (Materials and Method, Eqs 28 and 30).

Detailed regional relative errors are shown at three G values (S4C and S4D Fig). We noted that with the increase of G, reconstruction performance of w_i at all regions increased, while reconstruction performance of I_i shows variability, consistent with previous studies that also reported inaccurate I_i estimation [36].

To further examine whether the variability in reconstructed $\hat{I}_i$ significantly affects the dynamical system's ability to capture FC patterns, we re-simulated neural activity using the reconstructed parameters ($\hat{w}_i$, $\hat{I}_i$, and $\hat{C}_{ij}$) in Model A and compared the correlation between the re-simulated FC and the original ground truth FC. Our results demonstrate that even near the second bifurcation point ($G = 1.3$), the average correlation remains reasonable at 0.84, indicating that the inaccurate estimation of I_i does not substantially impair the framework's capacity to reproduce essential FC characteristics (S4B Fig, Solid line). Notably, re-simulation using a linear model (Eq. S1) with estimated effective heterogeneity $\hat{h}_i$ and

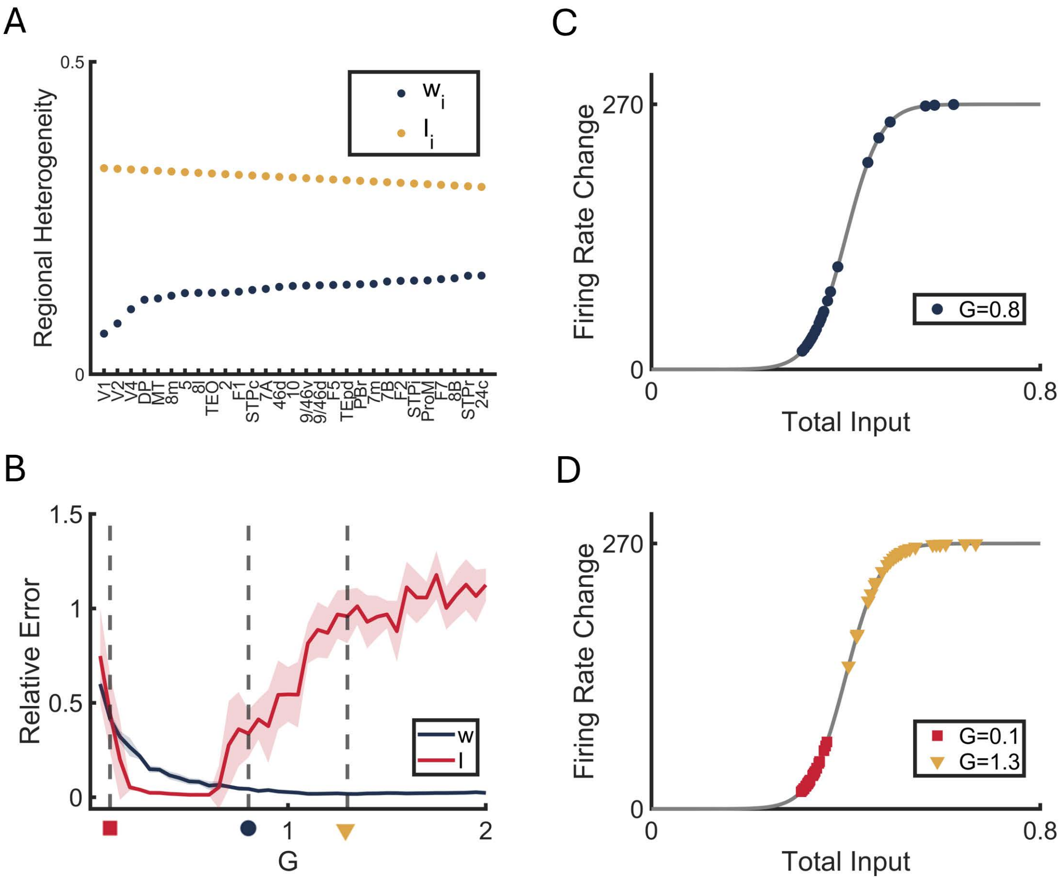

Fig 3. Performance in reconstruction of detailed parameters. (A) Ground truth features of Model A. The regional recurrent strength w_i is rescaled from empirical anatomical heterogeneity [43], while the external input I_i is set to decrease with hierarchy to be consistent with previous work [36]. **(B)** The relative errors in Model A between ground truth and estimation of w_i (blue) and I_i (red) as functions of G. Vertical dash lines represent different G values: $G = 0.1$ (red square), $G = 0.8$ (blue round) and $G = 1.3$ (yellow triangle). **(C and D)** Derivative of firing rate $\frac{dH}{dx_i}(x_i)$ at stable states S^* for each ROI under three different global coupling strengths corresponding to B. Firing rate change of each ROIs under high global coupling are located at nonlinear region (D, yellow triangle). The colored lines show the mean value across 10 simulations, with shaded areas indicating one standard deviation from the mean. Simulation length 50,000*s*.

https://doi.org/10.1371/journal.pcbi.1013612.g003

asymmetric SC $\hat{C}_{ij}$ successfully reproduces the FC patterns (S4B Fig, Dashed line). Together, these results suggest that our framework successfully captures the effective heterogeneity and asymmetric SC. Although detailed reconstruction of parameters suffers from nonlinearity, the reconstructed parameters can still reasonably reproduce the observed FC patterns.

V. Effective heterogeneity contributed by different heterogeneity and unobserved inhibitory dynamics

Our analysis of Model A presented above demonstrates that effective heterogeneity is influenced not only by anatomical heterogeneity but also by the underlying dynamical states (Table 2). However, heterogeneous large-scale circuit modeling in macaque and human studies have incorporated various experimental data reflecting regional variations, emphasizing the variability in parameterizing empirical heterogeneity into the dynamical properties of each region [36,37,43]. Therefore, we propose that the effective heterogeneity identified through our EC separation framework provides a unified approach to characterize the dynamical contributions of heterogeneity based on different empirical data sources.

We next sought to investigate whether this framework for detailed reconstruction could be applied to an alternative large-scale heterogeneous model where regional heterogeneity occurs in other parameters, including effective heterogeneity and asymmetric SC reconstruction in E-I model.

We first utilized a modified dynamical mean-field model (Model B) [37] in which heterogeneity was introduced in other local parameters, specifically the timescale τ_i and firing threshold b_i, which govern the regional capacity for information loss and accumulation, while local recurrent strength *w* and effective outer input *I* were uniform across regions [Materials and Method, Eqs 31–33]. The detailed reconstruction of timescale $\hat{\tau}_i$ and firing threshold $\hat{b}_i$ was computed using $\hat{h}_i$ and estimated EC $\hat{J}$.(Eqs 35 and 36).

We found that the ground truth τ_i and b_i of Model B can be calculated from Eq. S2 using ground truth w_i and I_i of Model A, which provides a mapping relationship between these parameter pairs of the two models. The homogeneous *w* and *I* of Model B are the averaged of ground truth w_i and I_i of Model A.

Similar to the results observed in Model A, the relative errors of both reconstructed asymmetric SC (Fig 4A, blue) and effective heterogeneity h_i (Fig 4A, red) decreased as the global coupling strength *G* increased. Furthermore, detailed reconstruction of the parameterized heterogeneity τ_i and b_i showed good estimation performance within a moderate range of *G* (Fig 4B). However, the relative reconstruction errors in Model B were higher than those in Model A, particularly at low values of *G*. This reveals that using τ_i as regional heterogeneity parameters may be more sensitive to noise.

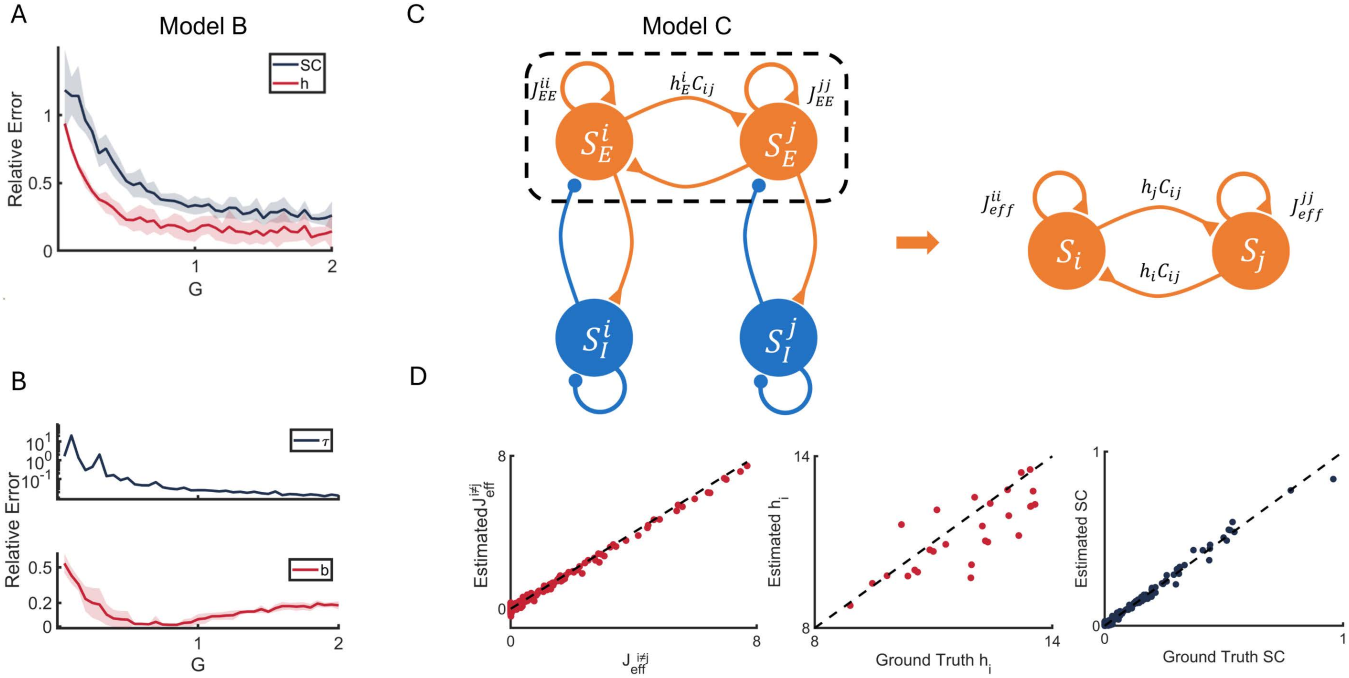

Fig 4. Reconstruction performance of Model B and Model C. (A) The relative errors of reconstruction of the asymmetric SC (blue) and regional heterogeneity h_i (red) of Model B as functions of *G*. **(B)** The relative errors between ground truth and estimation of τ_i (blue) and firing threshold b_i (red) of Model B as functions of *G*. **(C)** Illustration of reconstruction procedure with localized excitation-inhibition interactions (Model C). The full model consists of an excitatory S_E^i and an inhibitory population S_I^i for each region ($i = 1, \ldots, N$), and only excitatory populations have inter-region connections: $h_E^i C_{ij}$ represents the directed connection from region *j* to region *i*, with C_{ij} denotes the SC and h_E^i denotes the effective heterogeneity of excitatory population. J_{EE}^{ii} represents the local recurrent strength of the excitatory population of region ***i*****.** Dash square represents that only the activity of excitatory populations is observed for reconstruction. J_{eff}^{ii} represents the effective local recurrent strength reconstructed from excitatory activity and h_i is the effective heterogeneity absorbing the influence from inhibitory population. **(D)** Reconstruction example of Model C while only excitatory activity is observed. Ground truth J_{eff} and h_i are derived in Eqs 11 and 13. Dash line represents $y = x$.

https://doi.org/10.1371/journal.pcbi.1013612.g004

We also demonstrated that the heterogeneous parameters of Model A and Model B exhibit similar dynamical properties on shaping the effective heterogeneity h_i and localized dynamics (i.e., diagonal elements of the Jacobian matrices) and can be converted into one another. Specifically, in the spirit of dimensionless analysis, the heterogeneous w_i and I_i in Model A can be mapped onto the heterogeneous τ_i and b_i in Model B while maintaining the same steady states and Jacobian matrix (Eq. S2). This was done by comparing the Jacobian matrices of each model (Eqs 27 and 34) at the same neural activity level S^* [Materials and Method]. Consequently, the FC and autocorrelation timescales of the neural dynamics remain generally unchanged (see Supplementary Information, S5 Fig). This is because in the steady state, the FC and autocorrelation are determined by the Jacobian obeying the Lyapunov equation [44]. Intuitively, the heterogeneity in τ_i and b_i in Model B parallels the heterogeneity in w_i and I_i in Model A, as both sets of parameters control regional activity patterns. Variations in external input I_i shift the baseline firing in the activation function H, similar to the role of firing thresholds b_i. Meanwhile, heterogeneous local recurrent strength w_i modulates self-activation capability, functionally equivalent to the effect of decay time constants τ_i. This validates our proposed framework, where the effective heterogeneity h_i characterizes the dynamical contributions of different heterogeneous parameters and provides a top-down perspective on how to configure heterogeneous parameters to match empirically observed effective heterogeneity.

We next sought to extend our investigation by incorporating excitatory-inhibitory population dynamics to explore how inhibitory activity contributes to network reconstruction and modulates effective heterogeneity when only activity from the excitatory population is accessible. The balance between excitatory and inhibitory neural populations enriches the spatiotemporal patterns and stability of brain dynamics, underscoring the critical role of inhibitory populations in shaping sophisticated brain dynamics [43,46,47]. However, fluctuations of whole brain imaging data such as BOLD and magnetoencephalographic (MEG) signals are thought to be largely contributed by excitatory postsynaptic potentials rather than inhibitory postsynaptic potentials [48,49]. This physiological bias complicates the reconstruction of effective heterogeneity and connectivity asymmetry from such data.

Specifically, we analyzed the reconstruction performance of an excitatory-inhibitory mean-field model featuring a localized inhibitory population (Model C, Fig 4C). We consider the scenario where inhibitory activity is unobserved, and only excitatory activity is used for reconstruction, and quantify the influence of the inhibitory population on the estimation (Fig 4C). This approach allows us to examine the impact of inhibitory dynamics on effective heterogeneity and their role in shaping network-level properties.

We first characterize the reconstruction method of an excitatory-inhibitory model (Model C, Eqs 37–42) as similar in section II [38,50].

The linearized dynamics around the steady states S^* [Materials and Method]:

$$\frac{dS}{dt} = J_{S^*}\left(S - S^*\right) + \sigma\nu(t), \tag{10}$$

where $S = \begin{bmatrix} S_E \\ S_I \end{bmatrix}_{2N\times 1}$, and J_{S^*} is the full Jacobian matrix in the form of a block matrix [Materials and Method].

Here, $N = 29$ represents the number of cortical areas. For each cortical region with two populations (E/I), the Jacobian matrix J_{S^*} has $2N$ dimensions with four N-dimension blocks: $\begin{bmatrix} J_{EE} & J_{EI} \\ J_{IE} & J_{II} \end{bmatrix}_{2N\times 2N}$ where J_{pq} denotes the connections from population q to p, where $p, q \in \left\{E, I\right\}$. The top-left block J_{EE} represents the long-range excitation-to-excitation connectivity across regions, while J_{EI}, J_{IE} and J_{II} are diagonal matrices since only excitatory populations participate in inter-regional communications (Eq. 48).

We then derive the approximated ground truth J_{eff} of excitatory population S_E [Materials and Method]:

$$J_{eff} = J_{EE} - J_{EI}J_{II}^{-1}J_{IE}. \tag{11}$$

Because J_{EI}, J_{IE} and J_{II} are diagonal matrices (there is only long-range E-E connection), this absorption indicates that localized inhibitory populations mainly modulate the parameters of corresponding excitatory population of each region. Following Eq. 11, the ground truth effective Jacobian J_{eff} can be represented as effective heterogeneity and asymmetric SC (same as Eq. 5):

$$[J_{eff}]_{ij} = h_i C_{ij}, \tag{12}$$

with effective heterogeneity

$$h_i = \gamma G \left(1 - S_E^{i*}\right) g_E^i, \tag{13}$$

where $g_E^i = \frac{dH_E^i}{dx_E^i}|_{x_E^{i*}}$ is the firing rate change of excitatory population (gain function level).

Overall, Eq. 11 provides an approximated mathematical ground truth during the reconstruction when using only the excitatory activity S_E, enabling us to further test the separation of effective heterogeneity and asymmetric structural connectivity (Eqs 7–9, Fig 4D).

Previous studies have found that the best fit to empirical data occurs at the edge of Hopf bifurcation, representing a regime where stable dynamics coexist with oscillatory behavior [50,51]. To validate our prediction on effective Jacobian in Eq. 11 and whether our reconstruction method can still hold with only excitatory activity observations and symmetric SC, we simulated the model C with or without the feedback inhibition control (FIC, controlling that regional firing rates are ~ 3Hz, see also Eq. S4) and only kept the excitatory activity S_E^i of each region for the temporal (Eq. 7) and spatial reconstruction (Eq. 9).

Simulation results indicated good reconstruction performance in estimating the off-diagonal elements of effective Jacobian J_{eff} using only excitatory activity (Figs 4D and S6). Also, the diagonal elements of the estimated effective Jacobian are well aligned with our approximation in Eq. 11, further validating the precision of our approximation (S7 Fig).

Similarly, we characterized bifurcations in Model C under both FIC and non-FIC conditions. Our results demonstrate that even at bifurcations, we can achieve sufficiently good effective heterogeneity and asymmetry reconstruction (S6 Fig). Although we noted that determining the effective heterogeneity h_i and asymmetric SC C_{ij} only requires the excitatory activity S_E^i and symmetric SC W_{ij}, achieving further detailed reconstruction of parameterized heterogeneity w_{EE}^i and w_{IE}^i remains a challenge due to the lack of inhibitory population parameters.

Together, our results highlight the feasibility of mapping different parameterized heterogeneities onto their functional contributions as distinct components of effective heterogeneity, and demonstrate that this reconstruction method performs well in E-I networks with hidden local inhibitory populations. These analyses support the flexibility of heterogeneous modeling approaches in capturing the functional dynamics of large-scale brain networks.

VI. Sampling interval effect on estimating effective connectivity

A key question is how the underlying neural interactions inferred from neural activity depend on the temporal resolution of empirical data, which is hardly noticed in EC studies [26,48]. This mismatch between temporal resolutions might bring system errors in multi-modality comparisons (like MEG and fMRI signals) and pose significant challenges to the interpretation of the obtained EC. To address this, we investigated the influence of sampling resolution of the neural activity on temporal reconstruction performance and mathematically quantified the relationship between the sampling rate and the reconstructed Jacobian matrix. We began by discretizing the linear system described in Eq. 4 with a time step h:

$$\frac{x(t+h)-x(t)}{h} = J_o x(t) + \sigma\nu(t), \tag{14}$$

where $x(t) = S(t) - S^*$ represents the shifted neural activity and $J_o = J$ is the original Jacobian matrix at the stable fixed point S^*.

Due to technical limitations (e.g., fMRI detects BOLD signals at intervals on the order of hundreds of milliseconds), observed neural activity is sampled at a sampling step *n* with a time step *T*. Under these conditions, the discrete linear system can be represented in an exponentially diffused manner [Materials and Method] [48]:

$$\frac{x(t+T)-x(t)}{T} \approx \frac{e^{TJ_o}-I}{T}x(t) + B_T\nu(t). \tag{15}$$

The ground truth Jacobian matrix after sampling is expressed as:

$$J_T = \frac{e^{TJ_o}-I}{T}, \tag{16}$$

and the matrix estimated by temporal reconstruction is described as:

$$\hat{J}_T = < \frac{x(t+T)-x(t)}{T}, x(t) > \ < x(t), x(t) >^{-1} . \tag{17}$$

Eq. 16 illustrates how the temporal resolution of the sampled activity results in an exponential scaling of the true Jacobian matrix J_o at a rate determined by the sampled time step *T*. This occurs because the true dynamics evolve in the network between one sampling time step and the next, a phenomenon previously noted in studies inferring EC from fMRI time series [48]. Therefore, we have provided a ground truth EC under the sampling interval *T*, while using sampled neural activity for temporal reconstruction.

Then, the estimation of the true Jacobian matrix $\hat{J}_o$ is solved from Eq. 17 using matrix logarithm operation [Materials and Method]:

$$\hat{J}_o = \frac{\ln\left(T\hat{J}_T+I\right)}{T}. \tag{18}$$

We assessed the effect of sampling interval by examining the reconstructed matrix $\hat{J}_T$ from sampled neural activity across sampling time steps *T* ranging from 0.01s to 1s. The estimated matrix $\hat{J}_T$ was strongly correlated with the deduced exponential diffusion matrix J_T in Eq. 16 across different sampling steps (Fig 5A).

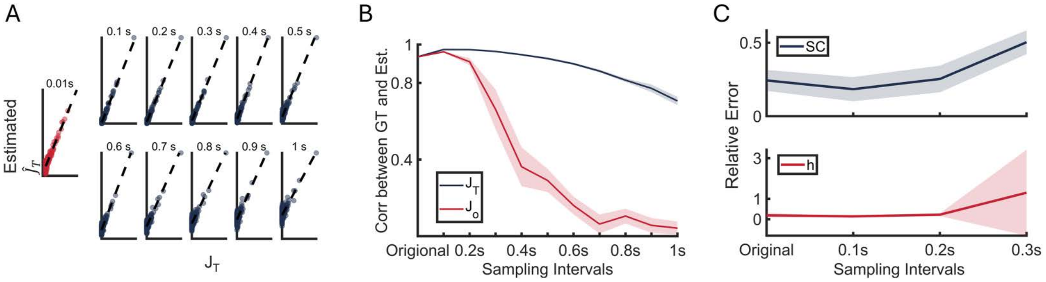

Fig 5. Reconstruction performance with respect to the sampling interval of observations. (A and B) Reconstruction and prediction of exponential scaling strongly match across sampling steps. (A) Element-wise comparison between estimated Exponential Jacobian $\hat{J}_T$ from sampled neural activity and analytical Jacobian J_T across different sampling resolution from 0.01s (unsampled, red) to 1s (100 steps, blue). Dash line represents $y = x$. (B) Correlation of $\hat{J}_T$ and J_T (blue), $\hat{J}_o$and J_o (red) across different sampling step *n*. (C) The relative errors between ground truth and estimation of asymmetric SC (blue) and effective heterogeneity h_i (red) estimated from $\hat{J}_o$ as functions of sampling steps. The colored lines show the mean relative errors across 10 simulations, with shaded areas indicating one standard deviation from the mean. Simulation length 50,000*s*.

https://doi.org/10.1371/journal.pcbi.1013612.g005

Both correlations of $\hat{J}_T$ and J_T, $\hat{J}_o$and J_o decreased as the sampling interval increased (Fig 5B). Notably, the correlation between the ground truth J_o and the estimated $\hat{J}_o$ (Fig 5B, red) declines more rapidly than that between J_T and $\hat{J}_T$ (Fig 5B, blue) at sampling interval of 0.3s or longer. This stronger decline can be attributed to two key factors. First, downsampling preferentially preserves strong connections while weak connections decay toward zero, as temporal precision and rapid neural activity changes are lost in the process. This effect, combined with estimation noise, leads to increased false positive rates at longer sampling intervals (Fig 5A, evidenced by greater scatter near zero). The transformation from $\hat{J}_T$ to $\hat{J}_o$ through the matrix logarithm operation further amplifies these effects (Fig 5B, red), reflecting the fundamental limitation in reconstructing network connectivity from low-temporal-resolution observations. Second, the estimation $\hat{J}_o = \frac{\ln\left(T\hat{J}_T+I\right)}{T} \in \mathrm{C}^{N\times N}$ is not uniquely defined under the matrix logarithm [48]. The solution's uniqueness is determined by both the asymmetry of $\hat{J}_T$ and the sampling interval T, leading to increased sparsity in J_T and consequently, non-unique solutions.

Further reconstruction of effective heterogeneity h_i and asymmetric SC C_{ij} from $\hat{J}_o$ demonstrated high precision in estimation for up to sampling interval of 0.2s (Fig 5C). However, the precision and stability of these estimations deteriorated at 0.3s, likely due to reduced accuracy in estimating the true Jacobian matrix $\hat{J}_o$.

Discussion

Local heterogeneity and asymmetry connections jointly shape the directionality of information flow in dynamical neural networks. In this study, we developed a reconstruction framework based on the existing directionality estimation method DDC to further separate local heterogeneity from asymmetric connections. Evaluation on dynamical mean field models as ground truth has shown that our approach effectively recognizes the existence of local heterogeneity and asymmetric connections through the directionality of the estimated Jacobian matrix and symmetric connection constraints. The separated heterogeneity revealed by this method quantifies how different forms of parameterized local heterogeneity together with the asymmetric connections alter whole brain dynamics. We also deduced a theoretical prediction on the effective interactions between excitatory populations with hidden inhibitory populations. Finally, we demonstrated the sampling interval effect with respect to temporal resolution in sampling the neural activity in observations in a linear dynamic framework. Collectively, our approach highlights the potential for segregating biophysical asymmetric structural connections and regional heterogeneity from neural activity.

The entangled local heterogeneity and asymmetric connections

Regional heterogeneity is crucial for generating and guiding information flow within the cortex. It supports functional segregation across structurally separated brain regions [37,38,43,52]. Experimental evidence suggests that regions with higher average pyramidal neuronal spine counts are thought to exhibit greater self-excitation and higher probability to act as source of activation spreading, representing the directionality of information transmission, enhancing information flow and contributing to the directionality of functional connectome [8,43,53]. This information directionality is also based on asymmetric SC, which captures richer feedforward and feedback details at the inter-regional level. This suggests that regional heterogeneity and asymmetric anatomical connections are entangled together, but little has been discussed in how they determine the directionality of the functional patterns [16–19]. Here, we propose a method that can separate and simultaneously estimate regional heterogeneity and asymmetrical structural connections. Specifically, this method estimates the directionality within the connectivity matrix and subsequently strips the regional heterogeneity of the brain network. Previously, based on the assumption of uniform regional dynamics, several theoretical approaches have been developed to estimate the directionality of connectomes, ranging from simple statistical inferring from functional connectivity to more sophisticated dynamical causal modelling leveraging hidden information within neural activity to uncover the directionality underlying neural activity [25–35].

It is important to note that our framework performs optimally in linear regimes where nonlinear interactions are not too strong. In highly nonlinear regimes, particularly where complex bifurcation dynamics emerge, parameter estimation becomes more challenging due to the nonlinear regimes in firing rate functions. However, even under these conditions, our approach maintains reasonable performance in capturing functional connectivity patterns, while still providing mechanistic insights through the decomposition of EC into effective heterogeneity and asymmetric SC.

Our method thus highlights the necessity to consider both regional heterogeneity and asymmetrical connections, thereby can be used for further probing their distinct functional roles in the whole brain dynamics.

Mapping anatomical and functional heterogeneity

Separated regional effective heterogeneity provides a quantitative mapping between anatomical and functional heterogeneity. While imaging studies have empirically detected various forms of anatomical heterogeneity [1–9,20] and are increasingly incorporating this data into large-scale circuit models [36–39,43,52], these studies have not been considered within a unified dynamical framework. Specifically, Chaudhuri et al. organized cortical areas in macaques based on laminar feedforward and feedback connections, embedding this heterogeneity into the excitatory input for all areas [43,52]. In contrast, Demirtaş et al. incorporated heterogeneity by embedding the T1w/T2w ratio into local recurrent strength [38], while Deco et al. focused on the role of gene expression of excitatory and inhibitory receptors in modifying the curvature of the activation function [37]. It was also shown that the gradient of synaptic inhibition, not the gradient of recurrent excitation, can well characterize the persistent activity patterns in the mouse cortex [39]. This raises the question: how different anatomical heterogeneity of intrinsic cortical features shape whole-brain dynamics?

We proposed to shift the focus to whether there are constraint rules for defining heterogeneous parameters in shaping dynamics. Our analysis revealed that effective heterogeneity can be systematically separated across different parameterized heterogeneity patterns. This consistency suggests a fundamental cause-and-effect relationship between anatomical and functional hierarchies, providing a framework for understanding mapping between different heterogeneity configurations. Importantly, we found that effective heterogeneity can be modulated by hidden inhibitory neuronal populations, which influence the overall level of network self-recurrence. This is equivalent to downscaling the entire network, while pairwise correlations are preserved through adjustments in the effective heterogeneity of EC [54]. Our method provides insights into how different parameterizations of heterogeneity can lead to similar functional outcomes in neural circuits.

While our linearized framework operates primarily in linear regimes, it successfully decomposes directional connectivity into neural activity-dependent effective heterogeneity and activity-independent asymmetric structural connectivity. Crucially, even in highly nonlinear regimes where parameter estimation becomes challenging, our approach maintains the ability to capture essential functional connectivity patterns, demonstrating robustness across different dynamical states. Although feedback inhibition control and the unique role of E-I populations (such as balanced amplification and oscillatory dynamics) are critical features that cannot be fully captured by linear approximations, our framework still provides a valuable approach for separating and estimating effective heterogeneity and asymmetric structural connectivity, offering fundamental insights into the constraint rules governing heterogeneous parameter organization and their impact on network dynamics.

Challenges in estimating directionality: Sampling interval effects of sampling rate and hemodynamics

Temporal resolution in sampling inconsistency of neural activity resolution leads to estimation bias. fMRI data from human subjects have facilitated the application of established theoretical methods to estimate the directionality of brain networks [26,27,33–35,55]. While this approach is prevalent in imaging neuroscience, BOLD signals suffer from poor temporal resolution, approximately 0.7-2 seconds [24–26]. This limitation can hinder the accurate detection of rapid neural dynamics and may compromise the reliability of directionality estimates, leading to spurious connections and false positives. Moreover, previous network inference studies [32,33,48,45] rarely consider the effects of sampling rate on the performance of estimating ground truth connectivity, which has limited their application to real data.

Here, we identified a sampling interval effect: the EC estimated from sampled data exhibits an exponential scaling relationship with the true SC. This effect occurs when there is a temporal resolution mismatch between the real neural activity (which we assume has dynamics with high temporal resolution) and the observed neural activity (sampled from the real neural activity at given intervals). For instance, when contrasting fMRI with MEG, the discrepancies may include sampling interval effects, thereby reducing the accuracy of EC estimation. This creates two challenges: (1) exponential scaling transforms the original structural connectivity into sampling interval dependent EC, causing weaker connections to decay while it preserves only the strongest interactions, and (2) the matrix logarithm transformation amplifies noise and can yield non-unique solutions to recover the original structural connectivity at longer intervals. Recent work has found that whole-brain pulse-response probability can be largely estimated by similar exponential scaling forms of SC, suggesting another interpretation of our work: the sampling interval effect also reveals the manner of information transmission during temporal intervals [56].

Despite active discussions in the engineering literature on overcoming this sampling issue—such as addressing the Nyquist frequency of the sampling rate and natural fluctuation rates—key aspects, such as comparing estimation methods with or without the matrix logarithm, remain underexplored and deserve further investigation [48]. Additionally, the estimation of matrix logarithm introduces technical challenges, as the existence and uniqueness of valid solutions are highly dependent on the structure of the connectivity matrix. Future directions may focus on developing approximation strategies and regularization techniques for matrix logarithm computation, which could potentially yield more accurate estimators and ensure robust solutions across different connectivity matrix structures. Consequently, although fMRI provides valuable insights into brain connectivity, the effects of BOLD signal resolution require careful consideration when interpreting findings related to brain network directionality.

In addition to the sampling interval effect, BOLD fMRI data presents another challenge: the hemodynamic response function convolves the underlying neural activity, creating temporal dependencies that obscure the direct relationship between neural dynamics and observed BOLD signals [57–59]. This hemodynamic convolution process systematically biases effective connectivity estimation because the observed BOLD signals represent a temporally smoothed and delayed version of the actual neural activity. The convolution process complicates the recovery of neural connectivity patterns, particularly for asymmetric connections where directionality and timing are crucial [48]. To address this limitation, future studies should incorporate hemodynamic response modeling directly into the connectivity estimation framework. This could be achieved through either deconvolution approaches that attempt to recover neural signals from BOLD data, or forward modeling approaches that explicitly account for hemodynamic convolution effects during connectivity estimation. Such methods have proven successful in calcium imaging, where deconvolution techniques are routinely used to infer neural activity from fluorescence signals [60–62].

Conclusion and outlooks

In conclusion, we proposed a method to simultaneously estimate local heterogeneity and asymmetric connections from observation of neural dynamics. Our findings provide a theoretical framework for further analysis of relative contributions of local heterogeneity and asymmetric connections to network dynamics.

Looking ahead, we will integrate multi-region MEG/sEEG datasets having high temporal resolution with symmetric structural connectivity from dMRI to uncover directional interactions between cortical areas and elucidate how local heterogeneity influences global brain function. We will pursue empirical validation by testing whether our effective heterogeneity measure correlates with region-specific features such as intrinsic timescales and neural variability in spiking dataset [63,64]. We suggest that effective heterogeneity may reflect the directionality of neural information flow, including top-down and bottom-up pathways, with directional flow switching potentially captured through variance in regional effective heterogeneity [65–67]. Additionally, we aim to investigate how the obtained asymmetric SC is related to the modular organization of the cortex – a key determinant of its functional segregation and integration [68,69].

By integrating our reconstruction framework with multimodal neuroimaging data, we can bridge gaps between anatomical organization and functional dynamics, ultimately advancing mechanistic models of how neural circuitry supports cognition and behavior.

Materials and method

1. Anatomical data

1A. Anatomical connectivity. The asymmetric SC used in dynamical modeling of the brain network is derived from a comprehensive project to quantitatively characterize all inter-areal connections in the macaque cortex [10], utilizing retrograde tracer injections to label projecting neurons and measuring connection strengths as fractional weights (fraction of labeled neurons). The anatomical connection from area *j* to area *i* is defined as the number of neurons projecting from area *j* to area *i*, normalized by the total number of neurons projecting from all areas to area *i*:

$$C_{ij} = \frac{\#\ neurons\ projecting\ from\ area\ j\ to\ area\ i}{\#\ neurons\ projecting\ from\ all\ areas\ to\ area\ i}.$$

In this research, we use 29 cortical areas reported from previous large-scale modeling studies that explored how asymmetric SC and anatomical hierarchy shape large-scale cortical dynamics [43,52]. The symmetric SC is defined as the average of asymmetric SC: $W = \frac{C+C^T}{2}$. This assumption aligns with dMRI-based SC, which can only detect fiber existence and density [21–23].

The asymmetry level $\eta(C)$ of the connectivity matrix C is calculated as the element-wise correlation between the upper and lower triangular matrices, quantifying the linear relationship between feedforward and feedback connections [70]: $\eta(C) = corr\,(C_{i>j}, C_{j>i})$.

We report that the asymmetry level of empirical macaque connectivity $\eta(C)$ is 0.7018, which represents that the connectivity matrix is symmetry-dominated but regulated by asymmetric connections.

1B. Regional heterogeneity implementation. The anatomical hierarchy is derived from the same dataset [15] using a generalized linear model that assigns hierarchical values based on the supragranular layer neuron fraction between cortical areas [15,43]. This anatomical hierarchy strongly correlates with T1w/T2w maps reflecting myelination [8]. Considering that T1w/T2w mapping is widely utilized in heterogeneous large-scale cortical modeling studies [36–38], we parameterized this anatomical hierarchy across the macaque cortex by incorporating region-specific local recurrent strength w_i into the model. External inputs I_i are chosen to sequentially decrease along the anatomical hierarchy, which are suggested to reflect the flow of sensory information from the external environment [36].

The range of w_i and I_i are scaled to $[0.0652, 0.1581]nA$ and $[0.33, 0.3]nA$ according to previous study on the same model [36].

2. Mathematical analysis

2A. Detailed Jacobian elements of Model A. In this section, we derive the Jacobian matrix of Model A (Eqs 1–3) around its steady state through Taylor expansion, retaining only the first-order terms. We further elaborate on the biological interpretation of the Jacobian matrix.

We start with the noise-driven nonlinear Model A (Eqs 1–3) and write it into a general nonlinear dynamic:

$$\frac{dS}{dt} = f(S;\theta) + \sigma\nu(t),$$

where θ represents system parameter and $\nu(t)$ is *i.i.d.* white noise. We then use Taylor expansion around steady state S^* and keep the first-order terms:

$$\frac{dS}{dt} = f(S^*;\theta) + \frac{\partial f(S;\theta)}{\partial S} \;|_{S=S^*} (S - S^*) + o\left(\frac{\partial f(S;\theta)}{\partial S}\right) + \sigma\nu(t)$$

$$\approx \frac{\partial f(S;\theta)}{\partial S} \;|_{S=S^*} (S - S^*) + \sigma\nu(t)$$

$$= J(S^*)(S - S^*) + \sigma\nu(t).$$

Here in the first line, $o(\frac{\partial f(S;\theta)}{\partial S})$ is the higher-order terms of Taylor expansion in the form of Peano's Remainder and is neglected in the following derivation. The Jacobian matrix $J(S^*) = \frac{\partial f(S;\theta)}{\partial S} \;|_{S=S^*}$ is the first order derivative of nonlinear function f near steady state S^*. The elements of Jacobian matrix are:

$$\begin{cases} J_{ii}(S^*) = -\frac{1}{\tau_S} - \gamma H(x_i)\,|_{x_i=x_i^*} + w_i\gamma(1 - S_i^*)\,\frac{\partial H}{\partial x_i}\,|_{x_i=x_i^*}\,, i = j \\ J_{ij}(S^*) = \gamma G(1 - S_i^*)\,C_{ij}\frac{\partial H}{\partial x_i}\;|_{x_i=x_i^*}\,, i \neq j \end{cases}. \tag{19}$$

The diagonal elements ($i=j$) describe how regional heterogeneity affects the self-regulation of each region: inherent time constant τ_s and regional firing rate $H(x_i)$, and the last term indicating recurrent excitation w_i, regional stable states S_i^* and regional firing rate change $\frac{dH}{dx}\;|_{x_i}$ entangle together to regulate the regional decay rate. Also, recurrent excitation w_i and external input I_i both contribute to the regional overall input x_i^*, therefore affect the regional firing rate $H(x_i)$ and firing rate change $\frac{dH}{dx}\;|_{x_i=x_i^*}$.

The off-diagonal elements ($i \neq j$) describe that the long-range communication from region j to region i is regulated by both the asymmetric projections C_{ij} and stable state $\{S_i^*, x_i^*\}$ of target region i. We noted that the difference of regional stable states still exists even in the absence of heterogeneity and asymmetry; this is because the graph properties (e.g., degree) of each region are different, but asymmetry and heterogeneity further enrich these dynamics [36–41,43].

2B. Procedure of temporal reconstruction and spatial reconstruction. Here, we provide mathematical details of how we process temporal reconstruction using DDC in Eq. 7 and spatial reconstruction to separate EC into effective heterogeneity and asymmetric SC in Eqs. We first took the outer product on both sides of Eq. 4 with S and average over time, yielding:

$$< \frac{dS}{dt}, S >= J < S, S >, \tag{20}$$

where J represents $J(S^*)$, $< S, S > =< S - S^*, S >$is the covariance matrix of neural activity, and $< \nu, S >\approx 0$ and is ignored, as shown in reference [35]. Here, the angle brackets$<,>$denote time averages.

Taking the inverse of covariance $< S, S >^{-1}$ on both sides, we derive the estimator for the Jacobian matrix which is asymmetrical in Eq. 7.

We next derive the multivariate least squares problem of spatial reconstruction in Eqs 8 and 9. We first reform Eq. 8 with $y_i = \frac{1}{h_i}$:

$$\hat{J}_{ij}y_i + \hat{J}_{ji}y_j = 2W_{ij},$$

and the corresponding vector form

$$M\,y\; = W_{vec}, \tag{21}$$

where $y_{N\times 1} = [y_1, y_2, \ldots, y_N]^T$, $M \in \mathcal{R}^{(N^2-N)\times N}$ is reform of $\hat{J}_{ij}$ and $\hat{J}_{ji}$, and $W_{vec} \in \mathcal{R}^{(N^2-N)\times 1}$ is the vectorized form of the non−diagonal elements of W. The estimation of y can then be solved using the following closed-form solution:

$$\hat{y} = (M^T M)^{-1} M^T W_{vec}. \tag{22}$$

Using $\hat{y}$, we can proceed to estimate effective heterogeneity $\hat{h}_i = \frac{1}{\hat{y}_i}$, and $\hat{C}_{ij} = \hat{y}_i \hat{J}_{ij}$.

2C. Spatial reconstruction without effective heterogeneity. To provide a baseline comparison for our method of simultaneously separating effective heterogeneity and asymmetric SC from estimated EC (i.e., Spatial Reconstruction), we first derived an optimization approach that ignores effective heterogeneity and considers only asymmetric SC. In this case, the asymmetry of Jacobian matrix is solely contributed from the asymmetry of SC and scaled by a constant h. In this baseline method, the inputs are the estimated EC (Jacobian) and symmetric SC, while the output is only the asymmetric SC.

We adjusted our original spatial reconstruction (Eqs 8 and 9) by treating the effective heterogeneity h_i to be homogeneous across regions:

$$\begin{cases} hC_{ij} = \hat{J}_{ij} \\ \frac{C_{ij}+C_{ji}}{2} = W_{ij} \end{cases}, \; i \neq j. \tag{23}$$

We then write the loss function L for optimizing C:

$$L(C; J, W) = \|J - hC\|_F^2 + \left\|C + C^T - 2W\right\|_F^2, \tag{24}$$

where $\|\cdot\|_F^2$ is the square of Frobenius norm quantifying the sum of least squares errors of matrix elements. The optimization was done by using *fmincon.m* in MATLAB.

The relative errors $RE\left(C_{ij}, \hat{C}_{ij}\right)$ are calculated across each G value for benchmark comparison during reconstruction of asymmetric SC.

2D. Spatial reconstruction without asymmetry. Above, we derived a baseline comparison that systematically ignores effective heterogeneity. Here, we consider an alternative baseline method where the directionality is entirely contributed by effective heterogeneity, while assuming the ground truth SC is symmetric. We adjusted the spatial reconstruction method (Eqs 8 and 9) by treating the asymmetric SC C_{ij} to be symmetric:

$$h_i W_{ij} = \hat{J}_{ij}, \; i \neq j. \tag{25}$$

In this case, we assume that the asymmetry of Jacobian matrix is purely contributed from the regional effective heterogeneity h_i. The estimation of each h_i is calculated:

$$\hat{h}_i = \left(W_{i,:}^T W_{i,:}\right)^{-1} W_{i,:}^T \hat{J}_{i,:},$$

where $W_{i,:} \in \mathcal{R}^{1,N}$ is the i-th row of symmetric SC W_{ij}, $\hat{J}_{i,:} \in \mathcal{R}^{1,N}$ is the i-th row of Jacobian $\hat{J}_{ij}$.

The relative errors between $RE\left(\hat{h}_i, h_i\right)$ are calculated for benchmark comparison during reconstruction of effective heterogeneity.

2E. Heterogeneity and asymmetry coupling reconstruction—Detailed spatial reconstruction of Model A. To further reconstruct the local circuit heterogeneity w_i, I_i and directed SC C_{ij} based on the estimated Jacobian matrix (EC) in the form of model A, we first need to approximate the diagonal terms of Jacobian matrix. By assuming $\frac{dS_i^*}{dt} \approx 0$ and neglecting the effect of noise input $\sigma\nu_i(t)$ in Eq. 1, we have:

$$\gamma H\left(x_i^*\right) = \frac{S_i^*}{\tau_s\left(1-S_i^*\right)} \tag{26}$$

Taking Eq. 26 into Eqs 5 and 6, the Jacobian Matrix $J(S^*)$ then can be expressed as:

$$\begin{cases} J_{ii}\left(S^*\right) = -\frac{1}{\tau_S\left(1-S_i^*\right)} + \frac{w_i h_i}{G}, i = j \\ J_{ij}\left(S^*\right) = h_i C_{ij}, i \neq j \end{cases} . \tag{27}$$

This approximation holds since the effect of noise fluctuation is relatively small near the fixed point S^*. Therefore, with Eqs 26 and 27, and recall that $y_i = \frac{1}{h_i} = \frac{1}{\gamma G J_N\left(1-S_i^*\right)\frac{\partial H}{\partial x_i}\ |_{x_i=x_i^*}}$, we can solve the local recurrent strength:

$$\hat{w}_i = G\hat{y}_i\hat{J}_{ii} + \frac{G\hat{y}_i}{\tau_S\left(1-S_i^*\right)}. \tag{28}$$

To reveal regional external input I_i, we use *fsolve.m* in MATLAB to solve for x_i^* from the derivative of activation function:

$$\frac{\partial H}{\partial x_i}|_{x_i=x_i^*} - \frac{1}{\gamma G\left(1-S_i^*\right)\hat{y}_i} = 0. \tag{29}$$

After estimating x_i^* and using Eq. 3, the regional external input I_i is calculated by the following formula:

$$\hat{I}_i = x_i^* - \hat{w}_i S_i^* - G\Sigma_j \hat{C}_{ij} S_j^*. \tag{30}$$

2F. Detailed spatial reconstruction of Model B. We seek to probe the ability of detailed reconstruction in an alternative large-scale circuit model (Model B) adapted from *Deco et al* [37]. From the perspective that the ability of accumulating and leaking information of each region varies, we define timescale τ_i and firing threshold b_i are heterogeneous in this model while keeping the local recurrent strength w and external input I homogeneous:

$$\frac{dS_i(t)}{dt} = -\frac{S_i}{\tau_i} + \gamma\left(1 - S_i\right)H\left(x_i\right) + \sigma\nu_i(t) \tag{31}$$

$$H_i\left(x_i\right) = \frac{ax_i - b_i}{1 - \exp\left(-d\left(ax_i - b_i\right)\right)} \tag{32}$$

$$x_i = wS_i + G\Sigma_j C_{ij} S_j + I, \tag{33}$$

where τ_i and b_i can represent the ability of leaking and storing information of each ROI.

Similarly, the Jacobian matrix J_B of Model B near steady state S^* in Eqs 31–33 can be derived:

$$\begin{cases} J_{B,ii}\left(S^*\right) = -\frac{1}{\tau_i\left(1-S_i^*\right)} + w\gamma\left(1 - S_i^*\right)\frac{\partial H_i}{\partial x_i}|_{x_i=x_i'}, i = j \\ J_{B,ij}\left(S^*\right) = \gamma G\left(1 - S_i^*\right)C_{ij}\frac{\partial H_i}{\partial x_i}|_{x_i=x_i'}, i \neq j \end{cases} . \tag{34}$$

We noted that the diagonal terms of J_B are approximated by assuming $\frac{dS_i^*}{dt} \approx 0$. In Model B, activation function H_i is heterogeneous across ROIs because of b_i and we defined $x_i' = wS_i^* + G\Sigma_j C_{ij} S_j^* + I$.

The detailed reconstruction follows the general reconstruction procedure of temporal reconstruction and spatial reconstruction as shown in Eq. 9 to reveal effective heterogeneity h_i^B and asymmetric connections $\hat{C}_{ij}$, we can therefore estimate

$$\frac{1}{\hat{\tau}_i} = (1 - S_i^*)\left(\frac{wh_i^B}{G} - J_{B,ii}\right), \tag{35}$$

and we also use *fsolve.m* in MATLAB to solve b_i from the derivative of activation function:

$$\frac{\partial H_i}{\partial x_i}|_{x_i=x_i'} - \frac{h_i^B}{\gamma G\left(1-S_i^*\right)} = 0. \tag{36}$$

The ground truth τ_i and b_i of Model B are calculated from Eq. S2 using ground truth w_i and I_i of Model A, which provides a mapping relationship between these parameter pairs. The homogeneous w and I of Model B are the average of ground truth w_i and I_i of Model A.

2G. Absorption of local inhibitory populations into effective Jacobian—Model C. Fluctuations in whole-brain imaging data such as BOLD and MEG signals are thought to largely reflect excitatory activity rather than inhibitory activity [48,49]. When estimating EC using such empirical data, the role of inhibitory populations is systematically neglected. A fundamental question arises: what exactly is the EC being reconstructed under these unobserved inhibitory dynamics? In this section, using Model C (E-I model) [38], we first derive an approximate solution for the ground truth EC when only excitatory activity is considered, and demonstrate how the estimated EC is affected by E-I interactions and subsequent decomposition for effective heterogeneity and asymmetric SC.

We introduce Model C considering both excitatory and inhibitory populations:

$$\frac{dS_E^i(t)}{dt} = -\frac{S_E^i}{\tau_E} + \gamma\left(1 - S_E^i\right) H_E\left(x_E^i\right) + \sigma\nu_E^i(t) \tag{37}$$

$$\frac{dS_I^i(t)}{dt} = -\frac{S_I^i}{\tau_I} + H_I\left(x_I^i\right) + \sigma\nu_I^i(t) \tag{38}$$

$$H_E\left(x_E^i\right) = \frac{a_E x_E^i - b_E}{1 - \exp\left(-d_E\left(a_E x_E^i - b_E\right)\right)} \tag{39}$$

$$H_I\left(x_I^i\right) = \frac{a_I x_I^i - b_I}{1 - \exp\left(-d_I\left(a_I x_I^i - b_I\right)\right)} \tag{40}$$

$$x_E^i = w_{EE}^i S_E^i + G\Sigma_j C_{ij} S_E^j - w_{EI} S_I^i + I_E, \tag{41}$$

$$x_I^i = w_{IE}^i S_E^i - S_I^i + I_I. \tag{42}$$

All parameters have the same properties as in model A and B but different in their values as listed in Table 3. For this model, we assume that the inhibition connections w_{EI}, are known and homogenous for different ROIs, and the local heterogeneity is attributed to excitatory connection w^i_{EE} and w^i_{IE} [38]. Here, we set w^i_{EE} and w^i_{IE} to increase linearly along the same anatomical hierarchy (Fig 3A) (Table 3).

To characterize the EC of the excitatory population in the presence of unobserved inhibitory populations, we mathematically reformulate the problem as an effective linear dynamical description of the excitatory population:

$$\frac{dS_E}{dt} = J_{eff}\left(S_E - S^*{}_E\right) + \sigma \nu_E(t), \tag{43}$$

where J_{eff} is the effective Jacobian matrix neglecting the modulation from inhibitory population as comared with the whole E-I network (Eqs 37–42). Consequently, when estimating EC using only excitatory activity, we can obtain an unbiased estimate of J_{eff}. Next, we seek to find the relationship between the ground truth effective Jacobian J_{eff} and the full Jacobian J_{S^*}, then the effective heterogeneity h_i and asymmetric SC C_{ij} under J_{eff}, as we did during the spatial reconstruction. Crucially, while J_{eff} and J_{S^*} both capture the same pairwise correlations within the excitatory population, they differ in dimensionality. We therefore derive the ground truth J_{eff} by leveraging the relationship between the Jacobian matrix and the covariance structure (unnormalized FC), which serves as the ground truth benchmark for evaluating our reconstruction approach in Section V.

According to Eq. 20, the linearized dynamics of S_E can be expressed as:

$$\frac{dS_E}{dt} = J_{EE}S_E + J_{EI}S_I + \sigma\nu_E,$$

take outer product of S_E and average over time, we have

$$< \frac{dS_E}{dt}, S_E >= J_{EE} < S_E, S_E > + J_{EI} < S_I, S_E >,$$

then take the inverse of $COV_{EE} =< S_E, S_E >$, we can express J_{eff} as:

$$J_{eff} =< \frac{dS_E}{dt}, S_E > < S_E, S_E >^{-1} = J_{EE} + J_{EI}COV_{IE}COV_{EE}^{-1}. \tag{44}$$

Compared to the estimation of reduced dynamics (Model A, Eq. 9), the estimation in Eq. 45 indicates that the inhibitory population in the dynamics will introduce a bias term in estimating EC: $J_{EI}COV_{IE}COV_{EE}^{-1}$. To illustrate what underlying matrix the J_{eff} is representing, we need to represent the covariance COV_{IE} and COV_{EE}^{-1} with block matrices of the full Jacobian J_{S^*}.

Table 3. Fixed parameters for large-scale excitatory-inhibitory circuit model (Model C).

Parameter	Excitatory Populations	Inhibitory Populations
τ_P	0.1 s	0.01 s
a_P	310 nC^{-1}	615 nC^{-1}
b_P	125 Hz	177 Hz
d_P	0.16 s	0.087 s
I_P	0.382 nA	0.2674 nA
w_{EI}	1	–
γ	0.641	–
w^i_{PE}	0.126 − 0.210 nA	0.090 − 0.150 nA

https://doi.org/10.1371/journal.pcbi.1013612.t003

To do so, we can represent the block matrices of the full covariance matrix ∑ with block matrices of Jacobian J_{S^*} by approximating $\Sigma = \sigma^2 J_{S^*}^{-1} J_{S^*}^{-T}$: letting $\frac{dS}{dt} = 0$, we have $S = -\sigma J_{S^*}^{-1}\nu$ and therefore $\Sigma = \langle S, S^T \rangle = \sigma^2 J_{S^*}^{-1} J_{S^*}^{-T}$. This approximation assumes that the instant change of activity remains near zero at a relatively low level of noise strength σ [71], providing a clear mapping relationship between the block matrices within the covariance ∑ and the full Jacobian J_{S^*}, then this can be derived from the following equation which provides a direction expression of how asymmetric Jacobian shapes steady covariance ∑ of the system [71]:

$$\Sigma = \sigma^2 J_{S^*}^{-1} J_{S^*}^{-T}, \tag{45}$$

where $\Sigma = \begin{bmatrix} COV_{EE} & COV_{EI} \\ COV_{IE} & COV_{II} \end{bmatrix}$ and with the knowledge of Schur Complement [72], we have:

$$J_{S^*}^{-1} = \begin{bmatrix} P_{EE} & -P_{EE} J_{EI} J_{II}^{-1} \\ -J_{II}^{-1} J_{IE} P_{EE} & J_{II}^{-1} + J_{II}^{-1} J_{IE} P_{EE} J_{EI} J_{II}^{-1} \end{bmatrix}$$

where we have $P_{EE} = \left(J_{EE} - J_{EI} J_{II}^{-1} J_{IE}\right)^{-1}$, and this implies that

$$COV_{EE} = \sigma^2 P_{EE} P_{EE}^T + \sigma^2 P_{EE} J_{EI}^2 J_{II}^{-2} P_{EE}^T,$$

$$COV_{IE} = -\sigma^2 J_{II}^{-1} J_{IE} P_{EE} P_{EE}^T - \sigma^2 J_{II}^{-1} J_{IE} P_{EE} J_{EI}^2 J_{II}^{-2} P_{EE}^T - \sigma^2 J_{II}^{-2} J_{EI} P_{EE}^T \approx -\sigma^2 J_{II}^{-1} J_{IE} P_{EE} P_{EE}^T - \sigma^2 J_{II}^{-1} J_{IE} P_{EE} J_{EI}^2 J_{II}^{-2} P_{EE}^T.$$

Therefore, we can solve that:

$$J_{EI} COV_{IE} COV_{EE}^{-1} \approx -J_{EI} J_{II}^{-1} J_{IE}. \tag{46}$$

Taking Eq. 46 in Eq. 44, we finally obtain the ground truth EC J_{eff} in Eq. 11.

The ground truth elements of EC J_{eff} is:

$$J_{eff} = \begin{cases} -\frac{1}{\tau_E} - \gamma H_E^{i*} + \gamma\left(1 - S_E^{i*}\right)\left(w_{EE} g_E^i - \frac{w_{EI} w_{IE} g_E^i g_I^i}{\frac{1}{\tau_I} + g_I^i}\right), i = j \\ \gamma G\left(1 - S_E^{i*}\right) g_E^i C_{ij}, i \neq j \end{cases}, \tag{47}$$

where $H_E^{i*} = H_E^i(x_E^{i*})$, and $g_P^i = \frac{dH_P^i}{dx_P^i} \mid_{x_P^{i*}}$ is the firing rate change (gain function level). For comparison, the full Jacobian matrix J_{S^*} is:

$$J_{S^*} = \begin{bmatrix} -\frac{1}{\tau_E} - \gamma H_E^{i*} + \gamma w_{EE}\left(1 - S_E^{i*}\right) g_E^i, \ i = j & -\gamma w_{EI}\left(1 - S_E^{i*}\right) g_E^i, \ i = j \\ \gamma G\left(1 - S_E^{i*}\right) g_E^i C_{ij}, \ i \neq j & 0, \ i \neq j \\ w_{IE} g_I^i, \ i = j & -\frac{1}{\tau_I} - g_I^i, \ i = j \\ 0, \ i \neq j & 0, \ i \neq j \end{bmatrix}. \tag{48}$$

2H. Sampling interval effect on EC reconstruction. In this section, we derive how sampling intervals affect EC estimation using Volterra expansion [73]. The Volterra expansion quantifies the impact of perturbations on nonlinear systems by expanding system responses before and after perturbation, where here noise serves as continuous perturbation influencing the neural dynamics. We start with the noise-driven nonlinear Model A (Eqs 1–3) and write it into a general nonlinear dynamic:

$$\frac{dx}{dt} = f(x;\theta) + \sigma\nu(t),$$

where θ represents system parameter and $v(t)$ is *i.i.d.* white noise. Apply the first-order Volterra expansion to the activity $x(t)$ at t_0 [73], we have:

$$x(t) = x(t_0) + \int_{t_0}^{t} f(x;\theta)dt' + \sigma\int_{t_0}^{t} K(t,t')\nu(t')\,dt' + O\left(\sigma^2\right), \tag{49}$$

where the first term is the initial state at t_0, the second term is the deterministic evolution (or zero-order Volterra kernel, representing the behavior of the dynamics when there is no outer input), $K(t,t') = \frac{\delta x(t)}{\delta\nu(t')}$ is the linear response function (Green's function of Model A, or the first-order Volterra kernel) and $\delta(\cdot)$ denotes functional derivative [5]. The last term $O\left(\sigma^2\right)$ denotes higher-order kernel with respect to the noise strength σ.

To have an explicit approximated solution of EC, we linearized this general nonlinear dynamic near its stable state x^* and we have:

$$\frac{dx}{dt} = J(x - x^*) + \sigma\nu(t).$$

We can calculate the linear response function according to the definition of Green's function [44]: $\left(\frac{d}{dt} - J\right)K(t,t') = \delta(t-t')$, this implies $K(t,t') = e^{J\left(t-t'\right)}$.

We then pick $t = t_0 + T$ represents the next time point after sampling at frequency $\frac{1}{T}$ (where $T = nh + \Delta \approx nh$, i.e., sampling activity every n time steps, $0 < \Delta < h$) and take the linear approximation into Eq. 49:

$$\begin{aligned} x(t_0+T) &\approx x^* + e^{JT}\left[x(t_0) - x^*\right] + \int_{t_0}^{t_0+T} e^{J\left(T+t_0-t'\right)}\nu(t')\,dt' \\ &= x^* + e^{JT}\left[x(t_0) - x^*\right] + \int_0^T e^{J(T-s)}\nu(s)ds \\ &\approx x^* + e^{JT}\left[x(t_0) - x^*\right] + B_T\nu(t_0+T), \end{aligned} \tag{50}$$

where in the last line, we simplify the white noise integral $\int_0^T e^{J(T-s)}\nu(s)ds$ into a mapping matrix B_T, where $B_T B_T^T = \sigma^2\int_0^T e^{Js}e^{J^Ts}ds$ [48]. Note that $\nu(t)$ represents Gaussian white noise with δ-correlation, the integral should be properly interpreted as an Itô stochastic integral with respect to a Wiener process. For brevity and since we consider only additive noise, we maintain the informal notation throughout [44]. Thus, we have derived how we naturally approximate the neural activity during the time interval $[t_0, t_0+T]$ [48].

We then use Eq. 50 to derive how this sampled neural activity contributes to EC estimation. We first minus $x(t_0)$ and devide by T at both sides:

$$\frac{x(t_0+T) - x(t_0)}{T} = \frac{e^{JT} - I}{T}\left[x(t_0) - x^*\right] + \frac{B_T}{T}\nu(t_0+T),$$

The ground truth EC at sampling interval T is calculated:

$$J_T = < \frac{x(t_0+T) - x(t_0)}{T}, x(t_0) > < x(t_0), x(t_0) >^{-1}$$

$$= < \frac{e^{JT} - I}{T}\left[x(t_0) - x^*\right] + \frac{B_T}{T}\nu(t_0+T), x(t_0) > < x(t_0), x(t_0) >^{-1}$$

$$= \left[< \frac{e^{JT} - I}{T}\left[x(t_0) - x^*\right], x(t_0) > + < \frac{B_T}{T}\nu(t_0+T), x(t_0) > \right] < x(t_0), x(t_0) >^{-1}$$

$$= < \frac{e^{JT}-I}{T}\left[x\left(t_0\right)-x^*\right], x\left(t_0\right) > < x\left(t_0\right), x\left(t_0\right) >^{-1}$$

$$= < \frac{e^{JT}-I}{T} x\left(t_0\right), x\left(t_0\right) > < x\left(t_0\right), x\left(t_0\right) >^{-1}$$

$$= \tfrac{e^{JT}-I}{T}, \tag{51}$$

where in the third line, the covariance $< \frac{B_T}{T}\nu\left(t_0+T\right), x\left(t_0\right) >= 0$ because of the independence of Gaussian white noise.

To estimate the true Jacobian matrix $\hat{J}_o$ from the reconstructed $\hat{J}_T$, we solved Eq. 16 as follows: rearrange Eq. 16 and take the matrix logarithm of both sides,

$$TJ_T = e^{TJ_o} - I,$$

$$\ln\left(TJ_T + I\right) = TJ_o,$$

then dividing by T we have isolated the J_o :

$$J_o = \frac{\ln\left(TJ_T + I\right)}{T}.$$

Substituting the estimated $\hat{J}_T$ using sampled neural activity in Eq. 17, we have the estimation of true EC in Eq. 18.

Supporting information

S1 Text. Supplementary methods. S1.1 Resimulation of Model A. S1.2 Mapping of Heterogeneity Pairs – Model A and Model B. S1.3 Implement of Feedback Inhibition Control. S1.4 Resimulation of Model C.
(DOCX)

S1 Fig. Robustness of reconstruction in effective heterogeneity and asymmetry. (A) The relative errors between ground truth and estimation of Jacobian as functions of data length. (B) The relative errors of estimated asymmetric SC (blue) and regional heterogeneity h_i (red) as functions of data length. (C) The mean and SD of effective heterogeneity h_i as functions of G. The mean of h_i monotonically increases as G increases, while SD of h_i shows a non-monotonous shape (first increase then decrease).
(TIF)

S2 Fig. Reconstruction performance in effective heterogeneity and asymmetry with/without ground truth properties. The relative errors of EC (A), effective heterogeneity (B) and asymmetric SC (C) reconstruction across four conditions where there is no ground truth asymmetry or heterogeneous parameter. All four conditions show comparable performance across different ground truth conditions as the global coupling G increases. Four ground truth models are considered for simulations: Heterogeneous parameters and asymmetric SC (He. Asym.); Homogeneous parameters and asymmetric SC (Ho. Asym.); Heterogeneous parameters and symmetric SC (He. Sym.); Homogeneous parameters and symmetric SC (Ho. Sym.). Heterogeneous parameters are w_i and I_i of Model A in the main text, homogeneous parameters are defined as the mean of w_i and I_i across regions.
(TIF)

S3 Fig. Robustness of reconstruction in effective heterogeneity and asymmetry using alternative EC estimations. (A) Example of iterative minimization of zero-lag and tau-lag covariance of neural activity through Lyapunov Optimization (LO) [4]. Color lines are the mean square error (MSE, defined as the Frobenius norm between estimate and ground truth as original research [4]) of the zero-lag covariance (blue), tau-lag covariance (yellow) and EC (red). (B) Reconstruction performance of estimating EC, where J_{LO} represents estimation using LO method. (C-E) Comparison of DDC and LO methods for estimating EC (C), effective heterogeneity (D), and asymmetric SC (E) across different G values. Our framework of separating EC into effective heterogeneity and asymmetric SC components demonstrates robust performance even under challenging conditions (e.g., G = 1) where LO encounters convergence difficulties. Tau-lag is chosen equal to τ_s. Shaded color represents 1-SD range across 10 times repetition.
(TIF)

S4 Fig. Detailed characterization of model performance and parameter estimation reliability. (A) Bistability across G. Each dot represents the stable firing rate of single region at every G. Red (Blue) dots are fixed points (FP) that start from lower (higher) initial states, representing lower (higher) stability. (B) Correlation between re-simulated FC and original FC. Solid line represents re-simulation of the model using reconstructed w_i and I_i and reconstructed asymmetric SC. Dash line represents re-simulation using effective heterogeneity and reconstructed asymmetric SC (Eq. S1). (C and D) Relative error of w_i and I_i across regions at three global coupling strength.
(TIF)

S5 Fig. Robustness of reconstruction in FC and timescale in mapping heterogeneous parameters. (A) Element-wise comparison between simulated FC from model A (heterogeneous w_i and I_i) and FC from model B (heterogeneous τ_i and b_i). (B) The resting state autocorrelation timescales of model A (blue) and model B (red) across ROIs. Here, we choose $G = 0.7$ as an example.
(TIF)

S6 Fig. Robustness of reconstruction in effective heterogeneity and asymmetry using E-I model. (A-C) Reconstruction of EC (A), effective heterogeneity (B) and asymmetric SC (C) using excitatory population activity simulated from E-I model with (solid line) or without FIC (dashed line). (D) Bifurcations of E-I models. Dashed line indicates where the E-I model exhibits a second fixed point (hollow gray circles). Dot-dashed line represents FIC instability, where firing rates cannot be controlled at 3Hz. (E) Intrinsic oscillation frequency calculated from imaginary eigenvalues divided by 2π. Eigenvalues are calculated by the Jacobian matrix at the fixed points. Dashed and dot-dashed lines correspond to the same conditions as in (D). (F) Correlations of FC between signals resimulated using estimated effective heterogeneity and asymmetry (Eq. S5) versus FC calculated from E population activity of the ground truth model.
(TIF)

S7 Fig. Diagonal analysis of Large-scale Balanced Network with Localized Inhibitory. Diagonal elements comparison for J_{EE} and modified effective Jacobian J_{eff} with estimated couplings $\hat{J}_E$ from the neural activity of excitatory population only. Here, we choose $G = 1.1$ as an example.
(TIF)

Acknowledgments

This research was conducted using the resources of the High Performance Computing Cluster Centre, HKBU, which receives funding from the RGC, University Grant Committee of Hong Kong and HKBU.

Author contributions

Conceptualization: Jiawen Chang, Zhuda Yang, Changsong Zhou.

Data curation: Jiawen Chang.

Formal analysis: Jiawen Chang.

Funding acquisition: Changsong Zhou.

Investigation: Jiawen Chang, Zhuda Yang.

Methodology: Jiawen Chang.

Project administration: Changsong Zhou.

Resources: Jiawen Chang.

Software: Jiawen Chang.

Supervision: Changsong Zhou.

Validation: Jiawen Chang.

Visualization: Jiawen Chang.

Writing – original draft: Jiawen Chang.

Writing – review & editing: Jiawen Chang, Zhuda Yang, Changsong Zhou.

References

1. Zilles K, Palomero-Gallagher N. Multiple Transmitter Receptors in Regions and Layers of the Human Cerebral Cortex. Front Neuroanat. 2017;11:78. https://doi.org/10.3389/fnana.2017.00078 PMID: 28970785
2. Nørgaard M, Beliveau V, Ganz M, Svarer C, Pinborg LH, Keller SH, et al. A high-resolution in vivo atlas of the human brain's benzodiazepine binding site of GABAA receptors. Neuroimage. 2021;232:117878. https://doi.org/10.1016/j.neuroimage.2021.117878 PMID: 33610745
3. Hansen JY, Shafiei G, Markello RD, Smart K, Cox SML, Nørgaard M, et al. Mapping neurotransmitter systems to the structural and functional organization of the human neocortex. Nat Neurosci. 2022;25(11):1569–81. https://doi.org/10.1038/s41593-022-01186-3 PMID: 36303070
4. Froudist-Walsh S, Xu T, Niu M, Rapan L, Zhao L, Margulies DS, et al. Gradients of neurotransmitter receptor expression in the macaque cortex. Nat Neurosci. 2023;26(7):1281–94. https://doi.org/10.1038/s41593-023-01351-2 PMID: 37336976
5. Dombrowski SM, Hilgetag CC, Barbas H. Quantitative architecture distinguishes prefrontal cortical systems in the rhesus monkey. Cereb Cortex. 2001;11(10):975–88. https://doi.org/10.1093/cercor/11.10.975 PMID: 11549620
6. Amunts K, Lepage C, Borgeat L, Mohlberg H, Dickscheid T, Rousseau M-É, et al. BigBrain: an ultrahigh-resolution 3D human brain model. Science. 2013;340(6139):1472–5. https://doi.org/10.1126/science.1235381 PMID: 23788795
7. Glasser MF, Van Essen DC. Mapping human cortical areas in vivo based on myelin content as revealed by T1- and T2-weighted MRI. J Neurosci. 2011;31(32):11597–616. https://doi.org/10.1523/JNEUROSCI.2180-11.2011 PMID: 21832190
8. Burt JB, Demirtaş M, Eckner WJ, Navejar NM, Ji JL, Martin WJ, et al. Hierarchy of transcriptomic specialization across human cortex captured by structural neuroimaging topography. Nat Neurosci. 2018;21(9):1251–9. https://doi.org/10.1038/s41593-018-0195-0 PMID: 30082915
9. Huntenburg JM, Bazin P-L, Goulas A, Tardif CL, Villringer A, Margulies DS. A Systematic Relationship Between Functional Connectivity and Intracortical Myelin in the Human Cerebral Cortex. Cereb Cortex. 2017;27(2):981–97. https://doi.org/10.1093/cercor/bhx030 PMID: 28184415
10. Markov NT, Ercsey-Ravasz MM, Ribeiro Gomes AR, Lamy C, Magrou L, Vezoli J, et al. A weighted and directed interareal connectivity matrix for macaque cerebral cortex. Cereb Cortex. 2014;24(1):17–36. https://doi.org/10.1093/cercor/bhs270 PMID: 23010748
11. Bazinet V, Hansen JY, Misic B. Towards a biologically annotated brain connectome. Nat Rev Neurosci. 2023;24(12):747–60. https://doi.org/10.1038/s41583-023-00752-3 PMID: 37848663
12. Shih C-T, Sporns O, Yuan S-L, Su T-S, Lin Y-J, Chuang C-C, et al. Connectomics-based analysis of information flow in the Drosophila brain. Curr Biol. 2015;25(10):1249–58. https://doi.org/10.1016/j.cub.2015.03.021 PMID: 25866397
13. Varshney LR, Chen BL, Paniagua E, Hall DH, Chklovskii DB. Structural properties of the Caenorhabditis elegans neuronal network. PLoS Comput Biol. 2011;7(2):e1001066. https://doi.org/10.1371/journal.pcbi.1001066 PMID: 21304930
14. Oh SW, Harris JA, Ng L, Winslow B, Cain N, Mihalas S, et al. A mesoscale connectome of the mouse brain. Nature. 2014;508(7495):207–14. https://doi.org/10.1038/nature13186 PMID: 24695228
15. Markov NT, Vezoli J, Chameau P, Falchier A, Quilodran R, Huissoud C, et al. Anatomy of hierarchy: feedforward and feedback pathways in macaque visual cortex. J Comp Neurol. 2014;522(1):225–59. https://doi.org/10.1002/cne.23458 PMID: 23983048
16. Deco G, Jirsa VK, McIntosh AR. Emerging concepts for the dynamical organization of resting-state activity in the brain. Nat Rev Neurosci. 2011;12(1):43–56. https://doi.org/10.1038/nrn2961 PMID: 21170073
17. Breakspear M. Dynamic models of large-scale brain activity. Nat Neurosci. 2017;20(3):340–52. https://doi.org/10.1038/nn.4497 PMID: 28230845

18. Fousek J, Rabuffo G, Gudibanda K, Sheheitli H, Petkoski S, Jirsa V. Symmetry breaking organizes the brain's resting state manifold. Sci Rep. 2024;14(1):31970. https://doi.org/10.1038/s41598-024-83542-w PMID: 39738729

19. Melozzi F, Bergmann E, Harris JA, Kahn I, Jirsa V, Bernard C. Individual structural features constrain the mouse functional connectome. Proc Natl Acad Sci U S A. 2019;116(52):26961–9. https://doi.org/10.1073/pnas.1906694116 PMID: 31826956

20. Glasser MF, Goyal MS, Preuss TM, Raichle ME, Van Essen DC. Trends and properties of human cerebral cortex: correlations with cortical myelin content. Neuroimage. 2014;93 Pt 2:165–75. https://doi.org/10.1016/j.neuroimage.2013.03.060 PMID: 23567887

21. Hagmann P, Cammoun L, Gigandet X, Meuli R, Honey CJ, Wedeen VJ, et al. Mapping the structural core of human cerebral cortex. PLoS Biol. 2008;6(7):e159. https://doi.org/10.1371/journal.pbio.0060159 PMID: 18597554

22. Wedeen VJ, Wang RP, Schmahmann JD, Benner T, Tseng WYI, Dai G, et al. Diffusion spectrum magnetic resonance imaging (DSI) tractography of crossing fibers. Neuroimage. 2008;41(4):1267–77. https://doi.org/10.1016/j.neuroimage.2008.03.036 PMID: 18495497

23. Jones DK. Challenges and limitations of quantifying brain connectivityin vivowith diffusion MRI. Imag Med. 2010;2(3):341–55. https://doi.org/10.2217/iim.10.21

24. Cole MW, Bassett DS, Power JD, Braver TS, Petersen SE. Intrinsic and task-evoked network architectures of the human brain. Neuron. 2014;83(1):238–51. https://doi.org/10.1016/j.neuron.2014.05.014 PMID: 24991964

25. Seguin C, Razi A, Zalesky A. Inferring neural signalling directionality from undirected structural connectomes. Nat Commun. 2019;10(1):4289. https://doi.org/10.1038/s41467-019-12201-w PMID: 31537787

26. Friston KJ. Functional and effective connectivity: a review. Brain Connect. 2011;1(1):13–36. https://doi.org/10.1089/brain.2011.0008 PMID: 22432952

27. Roebroeck A, Formisano E, Goebel R. Mapping directed influence over the brain using Granger causality and fMRI. Neuroimage. 2005;25(1):230–42. https://doi.org/10.1016/j.neuroimage.2004.11.017 PMID: 15734358

28. Seth AK, Edelman GM. Distinguishing causal interactions in neural populations. Neural Comput. 2007;19(4):910–33. https://doi.org/10.1162/neco.2007.19.4.910 PMID: 17348767

29. Stephan KE, Penny WD, Moran RJ, den Ouden HEM, Daunizeau J, Friston KJ. Ten simple rules for dynamic causal modeling. Neuroimage. 2010;49(4):3099–109. https://doi.org/10.1016/j.neuroimage.2009.11.015 PMID: 19914382

30. Novelli L, Friston K, Razi A. Spectral dynamic causal modeling: A didactic introduction and its relationship with functional connectivity. Netw Neurosci. 2024;8(1):178–202. https://doi.org/10.1162/netn_a_00348 PMID: 38562289

31. Fakhar K, Hilgetag CC. Systematic perturbation of an artificial neural network: A step towards quantifying causal contributions in the brain. PLoS Comput Biol. 2022;18(6):e1010250. https://doi.org/10.1371/journal.pcbi.1010250 PMID: 35714139

32. Zhang Z, Chen Y, Mi Y, Hu G. Reconstruction of dynamic networks with time-delayed interactions in the presence of fast-varying noises. Phys Rev E. 2019;99(4–1):042311. https://doi.org/10.1103/PhysRevE.99.042311 PMID: 31108723

33. Luo Z, Peng K, Liang Z, Xu Y, Guan Y, Cui X. Mapping effective connectivity by virtually perturbing a surrogate brain. Nat Methods. 2025.

34. Liégeois R, Santos A, Matta V, Van De Ville D, Sayed AH. Revisiting correlation-based functional connectivity and its relationship with structural connectivity. Netw Neurosci. 2020;4(4):1235–51. https://doi.org/10.1162/netn_a_00166 PMID: 33409438

35. Chen Y, Rosen BQ, Sejnowski TJ. Dynamical differential covariance recovers directional network structure in multiscale neural systems. Proc Natl Acad Sci U S A. 2022;119(24):e2117234119. https://doi.org/10.1073/pnas.2117234119 PMID: 35679342

36. Kong X, Kong R, Orban C, Wang P, Zhang S, Anderson K, et al. Sensory-motor cortices shape functional connectivity dynamics in the human brain. Nat Commun. 2021;12(1):6373. https://doi.org/10.1038/s41467-021-26704-y PMID: 34737302

37. Deco G, Kringelbach ML, Arnatkeviciute A, Oldham S, Sabaroedin K, Rogasch NC, et al. Dynamical consequences of regional heterogeneity in the brain's transcriptional landscape. Sci Adv. 2021;7(29):eabf4752. https://doi.org/10.1126/sciadv.abf4752 PMID: 34261652

38. Demirtaş M, Burt JB, Helmer M, Ji JL, Adkinson BD, Glasser MF, et al. Hierarchical Heterogeneity across Human Cortex Shapes Large-Scale Neural Dynamics. Neuron. 2019;101(6):1181-1194.e13. https://doi.org/10.1016/j.neuron.2019.01.017 PMID: 30744986

39. Ding X, Froudist-Walsh S, Jaramillo J, Jiang J, Wang X-J. Cell type-specific connectome predicts distributed working memory activity in the mouse brain. Elife. 2024;13:e85442. https://doi.org/10.7554/eLife.85442 PMID: 38174734

40. Deco G, Ponce-Alvarez A, Mantini D, Romani GL, Hagmann P, Corbetta M. Resting-state functional connectivity emerges from structurally and dynamically shaped slow linear fluctuations. J Neurosci. 2013;33(27):11239–52. https://doi.org/10.1523/JNEUROSCI.1091-13.2013 PMID: 23825427

41. Wang P, Kong R, Kong X, Liégeois R, Orban C, Deco G, et al. Inversion of a large-scale circuit model reveals a cortical hierarchy in the dynamic resting human brain. Sci Adv. 2019;5(1):eaat7854. https://doi.org/10.1126/sciadv.aat7854 PMID: 30662942

42. Abbott LF, Chance FS. Drivers and modulators from push-pull and balanced synaptic input. Prog Brain Res. 2005;149:147–55. https://doi.org/10.1016/S0079-6123(05)49011-1 PMID: 16226582

43. Chaudhuri R, Knoblauch K, Gariel M-A, Kennedy H, Wang X-J. A Large-Scale Circuit Mechanism for Hierarchical Dynamical Processing in the Primate Cortex. Neuron. 2015;88(2):419–31. https://doi.org/10.1016/j.neuron.2015.09.008 PMID: 26439530

44. Gardiner CW. Handbook of stochastic methods for physics, chemistry and the natural sciences. 2nd ed. Berlin: Springer-Verlag; 1985.

45. Gilson M, Moreno-Bote R, Ponce-Alvarez A, Ritter P, Deco G. Estimation of Directed Effective Connectivity from fMRI Functional Connectivity Hints at Asymmetries of Cortical Connectome. PLoS Comput Biol. 2016;12(3):e1004762. https://doi.org/10.1371/journal.pcbi.1004762 PMID: 26982185

46. Deco G, Ponce-Alvarez A, Hagmann P, Romani GL, Mantini D, Corbetta M. How local excitation-inhibition ratio impacts the whole brain dynamics. J Neurosci. 2014;34(23):7886–98. https://doi.org/10.1523/JNEUROSCI.5068-13.2014 PMID: 24899711

47. Liang J, Yang Z, Zhou C. Excitation–inhibition balance, neural criticality, and activities in neuronal circuits. Neuroscientist. 2024.

48. Valdes-Sosa PA, Roebroeck A, Daunizeau J, Friston K. Effective connectivity: influence, causality and biophysical modeling. Neuroimage. 2011;58(2):339–61. https://doi.org/10.1016/j.neuroimage.2011.03.058 PMID: 21477655

49. Gutschalk A, Hämäläinen MS, Melcher JR. BOLD responses in human auditory cortex are more closely related to transient MEG responses than to sustained ones. J Neurophysiol. 2010;103(4):2015–26. https://doi.org/10.1152/jn.01005.2009 PMID: 20107131

50. Deco G, Ponce-Alvarez A, Hagmann P, Romani GL, Mantini D, Corbetta M. How local excitation-inhibition ratio impacts the whole brain dynamics. J Neurosci. 2014;34(23):7886–98. https://doi.org/10.1523/JNEUROSCI.5068-13.2014 PMID: 24899711

51. Deco G, Kringelbach ML, Jirsa VK, Ritter P. The dynamics of resting fluctuations in the brain: metastability and its dynamical cortical core. Sci Rep. 2017;7(1):3095. https://doi.org/10.1038/s41598-017-03073-5 PMID: 28596608

52. Joglekar MR, Mejias JF, Yang GR, Wang X-J. Inter-areal Balanced Amplification Enhances Signal Propagation in a Large-Scale Circuit Model of the Primate Cortex. Neuron. 2018;98(1):222-234.e8. https://doi.org/10.1016/j.neuron.2018.02.031 PMID: 29576389

53. Elston GN. Specialization of the neocortical pyramidal cell during primate evolution. In: Kaas JH, editor. Evolution of nervous systems. Oxford: Academic Press; 2007. p. 191–242.

54. van Albada SJ, Helias M, Diesmann M. Scalability of Asynchronous Networks Is Limited by One-to-One Mapping between Effective Connectivity and Correlations. PLoS Comput Biol. 2015;11(9):e1004490. https://doi.org/10.1371/journal.pcbi.1004490 PMID: 26325661

55. Zhang Z, Zheng Z, Niu H, Mi Y, Wu S, Hu G. Solving the inverse problem of noise-driven dynamic networks. Phys Rev E Stat Nonlin Soft Matter Phys. 2015;91(1):012814. https://doi.org/10.1103/PhysRevE.91.012814 PMID: 25679664

56. Seguin C, Jedynak M, David O, Mansour S, Sporns O, Zalesky A. Communication dynamics in the human connectome shape the cortex-wide propagation of direct electrical stimulation. Neuron. 2023;111(9):1391–401.

57. Glover GH. Deconvolution of impulse response in event-related BOLD fMRI. Neuroimage. 1999;9(4):416–29. https://doi.org/10.1006/nimg.1998.0419 PMID: 10191170

58. Bailes SM, Gomez DEP, Setzer B, Lewis LD. Resting-state fMRI signals contain spectral signatures of local hemodynamic response timing. Elife. 2023;12:e86453. https://doi.org/10.7554/eLife.86453 PMID: 37565644

59. Gomez DEP, Polimeni JR, Lewis LD. The temporal specificity of BOLD fMRI is systematically related to anatomical and vascular features of the human brain. Imaging Neurosci (Camb). 2024;2:imag–2–00399. https://doi.org/10.1162/imag_a_00399 PMID: 40800285

60. Vogelstein JT, Packer AM, Machado TA, Sippy T, Babadi B, Yuste R, et al. Fast nonnegative deconvolution for spike train inference from population calcium imaging. J Neurophysiol. 2010;104(6):3691–704. https://doi.org/10.1152/jn.01073.2009 PMID: 20554834

61. Pnevmatikakis EA, Soudry D, Gao Y, Machado TA, Merel J, Pfau D, et al. Simultaneous Denoising, Deconvolution, and Demixing of Calcium Imaging Data. Neuron. 2016;89(2):285–99. https://doi.org/10.1016/j.neuron.2015.11.037 PMID: 26774160

62. Friedrich J, Zhou P, Paninski L. Fast online deconvolution of calcium imaging data. PLoS Comput Biol. 2017;13(3):e1005423. https://doi.org/10.1371/journal.pcbi.1005423 PMID: 28291787

63. Ito T, Brincat SL, Siegel M, Mill RD, He BJ, Miller EK, et al. Task-evoked activity quenches neural correlations and variability across cortical areas. PLoS Comput Biol. 2020;16(8):e1007983. https://doi.org/10.1371/journal.pcbi.1007983 PMID: 32745096

64. Murray JD, Bernacchia A, Freedman DJ, Romo R, Wallis JD, Cai X, et al. A hierarchy of intrinsic timescales across primate cortex. Nat Neurosci. 2014;17(12):1661–3. https://doi.org/10.1038/nn.3862 PMID: 25383900

65. Honey CJ, Newman EL, Schapiro AC. Switching between internal and external modes: A multiscale learning principle. Netw Neurosci. 2017;1(4):339–56. https://doi.org/10.1162/NETN_a_00024 PMID: 30090870

66. Bolt T, Nomi JS, Bzdok D, Salas JA, Chang C, Thomas Yeo BT, et al. A parsimonious description of global functional brain organization in three spatiotemporal patterns. Nat Neurosci. 2022;25(8):1093–103. https://doi.org/10.1038/s41593-022-01118-1 PMID: 35902649

67. Nobre AC, Gresch D. How the brain shifts between external and internal attention. Neuron. 2025.

68. Wang R, Lin P, Liu M, Wu Y, Zhou T, Zhou C. Hierarchical Connectome Modes and Critical State Jointly Maximize Human Brain Functional Diversity. Phys Rev Lett. 2019;123(3):038301. https://doi.org/10.1103/PhysRevLett.123.038301 PMID: 31386449

69. Wang R, Liu M, Cheng X, Wu Y, Hildebrandt A, Zhou C. Segregation, integration, and balance of large-scale resting brain networks configure different cognitive abilities. Proc Natl Acad Sci U S A. 2021;118(23):e2022288118. https://doi.org/10.1073/pnas.2022288118 PMID: 34074762

70. Martí D, Brunel N, Ostojic S. Correlations between synapses in pairs of neurons slow down dynamics in randomly connected neural networks. Phys Rev E. 2018;97(6–1):062314. https://doi.org/10.1103/PhysRevE.97.062314 PMID: 30011528

71. Tononi G, Sporns O, Edelman GM. A measure for brain complexity: relating functional segregation and integration in the nervous system. Proc Natl Acad Sci U S A. 1994;91(11):5033–7. https://doi.org/10.1073/pnas.91.11.5033 PMID: 8197179

72. Zhang F. The Schur complement and its applications. Springer Science & Business Media; 2006.

73. Volterra V. Theory of functionals and of integral and integro-differential equations. New York: Dover; 1959.